OPTIMIZATION AND COMPARISON OF THE LIQUID COOLING PLATE USED IN THE ELECTRIC VEHICLE BATTERY WITH DIFFERENT COOLANTS AS WATER AND ETHYLENE GLYCOL-WATER SOLUTIONS

Zehra Nihan ALINCA

T.C.
BURSA ULUDAĞ UNIVERSITY
GRADUATE SCHOOL OF NATURAL AND APPLIED SCIENCES

OPTIMIZATION AND COMPARISON OF THE LIQUID COOLING PLATE USED IN THE ELECTRIC VEHICLE BATTERY WITH DIFFERENT COOLANTS AS WATER AND ETHYLENE GLYCOL-WATER SOLUTIONS

Zehra Nihan ALINCA

Orcid no: 0009-0007-0899-8425

Prof. Dr. Muhsin KILIÇ
(Supervisor)

Orcid no: 0000-0003-2113-4510

MSc THESIS
DEPARTMENT OF MECHANICAL ENGINEERING

BURSA – 2023
All Rights Reserved

ÖZET

Yüksek Lisans Tezi

ELEKTRİKLİ ARAÇ BATARYASINDA KULLANILAN SIVI SOĞUTMA PLAKASININ SU VE ETİLEN GLİKOL-SU ÇÖZELTİLERİ OLARAK FARKLI SOĞUTUCULAR İLE OPTİMİZASYONU VE KARŞILAŞTIRILMASI

Zehra Nihan ALINCA

Bursa Uludağ Üniversitesi
Fen Bilimleri Enstitüsü
Makine Mühendisliği Anabilim Dalı

Danışman: Prof. Dr. Muhsin KILIÇ

Elektrikli araçlar, iklim değişikliğinin yıkıcı etkilerini en aza indirmek ve sürdürülebilir bir yaşam sağlamak amacıyla giderek yaygınlaşmaktadır. Bu araçlarda kullanılan bataryanın kullanım sırasındaki sıcaklığı, batarya performansını ve ömrünü doğrudan etkilemektedir. Bu nedenle sıcaklığı kontrol altına alan sistemler üzerindeki çalışmalar giderek artmaktadır.

Bu çalışmada Goupil G6 aracında kullanılan lithium ion batarya esas alınmış ve sabit ısı akısı sınır şartı için gerekli olan değeri bulmak adına bataryanın genel bir termal modeli Amesim ortamında oluşturulmuş ve validasyonu sağlanmıştır. 3020 [W/m²] ısı üreten ve 450 [mm] x 810 [mm] taban yüzey alanına sahip olan batarya için yine aynı taban yüzey alanına sahip soğutma plakası modellenmiştir. Çalışmada üç farklı kanal sayısı, kanal yükseklikleri ve akışkan debisi ile laminer ve türbülanslı koşullar altında optimizasyon çalışmaları gerçekleştirilmiştir. Buna ek olarak her bir farklı soğutucu akışkanları etkisini gözlemlemek için su ve etilen-glikolun iki farklı orandaki su ile karışımı incelenmiştir. Optimizasyon için Taguchi ortogonal matrisinden yararlanılmıştır ve analizler Hesaplamalı Akışkanlar Dinamiği (HAD) kullanılarak gerçekleştirilmiştir. Değerlendirme ölçütü olarak tabanda oluşan maksimum sıcaklık, taban yüzey sıcaklığının standart sapması ve basınç kaybı göz önünde bulundurulmuş, elde edilen çıktılar Minitab yazılımı kullanılarak değerlendirilmiştir. Birden fazla sonuç parametresi olduğu için Taguchi tabanlı çok yanıtlı Gri İlişki Analizi ile optimizasyon çalışması gerçekleştirilmiştir.

Anahtar Kelimeler: HAD, Elektrikli Araç Bataryası, Optimizasyon, Soğutma
2023, vii + 77 sayfa.

ABSTRACT

MSc Thesis

OPTIMIZATION AND COMPARISON OF THE LIQUID COOLING PLATE USED IN THE ELECTRIC VEHICLE BATTERY WITH DIFFERENT COOLANTS AS WATER AND ETHYLENE GLYCOL-WATER SOLUTIONS

Zehra Nihan ALINCA

Bursa Uludağ University
Graduate School of Natural and Applied Sciences
Department of Mechanical Engineering

Supervisor: Prof. Dr. Muhsin KILIÇ

Electric vehicles are becoming increasingly common in order to minimize the devastating effects of climate change and to provide a sustainable life. The temperature of the battery used in these vehicles directly affects the battery performance and life. For this reason, studies on systems that control the temperature are increasing.

In this study, the lithium ion battery used in the Goupil G6 vehicle is based, and a general thermal model of the battery was created and validated in the Amesim environment in order to find the required value for the constant heat flux boundary condition. For the battery producing 3020 [W/m²] heat and having a base surface area of 450 [mm] x 810 [mm], a cooling plate with the same base surface area is modeled. In the study, optimization studies were carried out under laminar and turbulent conditions with three different channel numbers, channel heights and fluid flow rate. In addition, to observe the effect of each different refrigerant, the mixture of water and ethylene-glycol with two different ratios and water was investigated. The Taguchi orthogonal matrix was used for optimization and analyzes were performed using Computational Fluid Dynamics (CFD). The maximum temperature, standard deviation of the surface temperature and pressure loss at the base were taken into account as evaluation criteria, and the outputs were evaluated using Minitab software. Since there is more than one result parameter, optimization study was carried out with Taguchi-based multi-response Grey Relational Analysis.

Key words: CFD, Electric Vehicle Battery, Optimization, Cooling
2023, vii + 77 pages.

ACKNOWLEGDEMENT

I would like to express my gratitude to Prof. Dr. Muhsin KILIÇ for guiding me throughout this thesis and passing on valuable information throughout my education.

Apart from my advisor: I would like to thank other faculty members, especially Assoc. Prof. M. Özgün KORUKÇU, for their valuable information and guidance. I am deeply thankful to Sevgül GAMSIZ for her support during the study.

My sincere thanks also go to Sylvain DE OLIVEIRA and Anthony DUPOUY for offering me the internship opportunity in their amazing team.

Last but not the least, I would like to thank my family and Sumer Tunçay for their encouragement and support throughout my journey.

Zehra Nihan ALINCA
15/06/2023

CONTENTS

Page

ÖZET i
ABSTRACT ii
ACKNOWLEDGEMENT iii
SYMBOLS and ABBREVIATIONS v
FIGURES vi
TABLES vii
1. INTRODUCTION 1
2. THEORETICAL BASICS AND LITERATURE REVIEW 4
2.1. General Background 4
2.1.1. Ansys Fluent and Amesim Software 4
2.1.2. Environmental Background 5
2.2. Theoretical Background 14
2.2.1. Lithium-ion Battery 14
2.2.2. Battery Thermal Management Systems 17
2.2.2.1. Air Cooling 18
2.2.2.2. Liquid Cooling 19
2.2.2.3. PCM Cooling 20
2.3. Previous Studies 21
3. MATERIALS AND METHOD 25
3.1. Validation Study 25
3.2. General Description of the Problem and Physical Model 31
3.2.1. Assumptions 34
3.3. Computational Fluid Dynamics (CFD) 35
3.4. Numerical Model 37
3.4.1. Mesh Independence Study 37
3.4.2. Boundary Conditions and Conservation Equations 39
3.5. Turbulence Model 40
3.5.1. Reynolds-Averaged Navier-Stokes (RANS) 41
3.6. Design of Experiment 43
3.6.1. Design of Experiment with Classical Methodology 43
3.6.2. Design of Experiment with Statistical Methodology 44
3.6.3. Creation of the Taguchi Statistical Design 50
3.7. One-dimensional Generic Model of the Battery 53
4. RESULTS AND DISCUSSION 57
5. CONCLUSION 70
REFERENCES 72
RESUME 77

SYMBOLS and ABBREVIATIONS

Symbols	Definition
A	Surface area of the heat flux surface
C	Battery charge rate
C_p	Specific heat of the fluid
D_h	Hydraulic diameter
g	Gravitational acceleration
q	Heat flux applied to the bottom of the plate
P_{fluid}	Area weighted average total pressure
P_{inlet}	Inlet pressure
P_{outlet}	Outlet pressure
$R_{thermal}$	Thermal resistance
Re	Reynolds number
T_{avg}	Mean temperature on the heat flux surface
T_σ	Standard deviation of temperature on the heat flux surface
T_{inlet}	Inlet temperature
T_{max}	Maximum temperature of the heat flux surface
u	Velocity vectors in the x direction
u_m	Average flow velocity
v	Velocity vectors in the y direction
W_{pump}	Pump power required to operate the system
w	Velocity vector in the z direction
ΔP	Pressure difference
μ	Dynamic viscosity
ρ	Density
ν	Kinematic viscosity
V	Volumetric flow rate

Abbreviation	Definition
BEV	Battery electric vehicle
BTMS	Battery thermal management systems
ETS	Economic transition scenario
EV	Electric vehicle
GHG	Greenhouse gases
GWP	Global warming potential
ICEV	Internal combustion engine vehicle
LES	Large eddy simulation turbulence model
PCM	Phase change material
PHEV	Plug-in hybrid electric vehicle
SOH	State of health

FIGURES

Page

Figure 2.1. Percentage of CO_2 production depending on the sectors..... 6Figure 2.2. CO_2 emissions in the transportation sector..... 7
Figure 2.3. GHG emissions and warming scenarios 8
Figure 2.4. Regional rates of BEV and PHEV between 2010 to 2021 9
Figure 2.5. Global EV fleet size predictions 9
Figure 2.6. Fleet predictions by countries according to ETS 10
Figure 2.7. Life cycle of an electric vehicle..... 11
Figure 2.8. Percentage of carbon emissions produced by ICEV, PHEV and BEVs during their life cycle 11
Figure 2.9. Distribution of GHG emissions by European countries 13
Figure 2.10. Schematic representation of the working principle of lithium-ion battery 14
Figure 2.11. Active and passive air cooling.....18
Figure 2.12. Passive liquid cooling system.....19
Figure 2.13. Active liquid cooling system 20
Figure 3.1. Validation geometry before slice operation.....26
Figure 3.2. Validation geometry after slice operation.....26
Figure 3.3. The mesh structure of the geometry 27
Figure 3.4. Detailed view of the mesh structure of the geometry 27
Figure 3.5. Name selection for validation study 28
Figure 3.6. Imported validation geometry to the fluent component.....29
Figure 3.7. 3D geometry of 4-channel cooling plate.....32
Figure 3.8. 3D geometry of 5-channel cooling plate.....32
Figure 3.9. 3D geometry of 6-channel cooling plate.....33
Figure 3.10. Steps of CFD analysis.....37
Figure 3.11. Mesh independence study.....38
Figure 3.12. Obtained mesh structure 38
Figure 3.13 Obtained mesh structure in detail 39
Figure 3.14. Stages of the classical methodology 44
Figure 3.15. Charge/discharge testbench model of G6 battery 53
Figure 3.16. Battery pre-sizing tool 54
Figure 3.17. Potential graph for AMESIM model 55
Figure 3.18. Potential graph for testbench 55
Figure 3.19. Obtained constant heat flux value.....56
Figure 4.1. Temperature contour on water cooled heat flux surface under laminar flow condition 66
Figure 4.2. Temperature distributions on the heat flux surface of the block in the arrays that give the best results (a) L8 for fluid water (b) L8 for fluid EGW 25 (c) L9 for fluid EGW 50 67

TABLES

Pages

Table 2.1.	Types of li-ion battery.....	16
Table 3.1.	Coolant properties used in validation study	30
Table 3.2.	Comparison of the results from the validation study	31
Table 3.3.	Thermal properties of Al.....	33
Table 3.4.	Thermal properties of EGW – 25%	34
Table 3.5.	Thermal properties of EGW – 50%	34
Table 3.6.	Thermal properties of water.....	41
Table 3.7.	Values used in the study	46
Table 3.8.	Flow type conditions depending on Reynolds number	50
Table 3.9.	Taguchi's orthogonal array table	51
Table 3.10.	Level combinations in the Taguchi L9 statistical design	51
Table 3.11.	Orthogonal array for laminar study.....	52
Table 3.12.	Orthogonal array for turbulent study	56
Table 4.1.	Result values obtained under laminar flow conditions	57
Table 4.2.	Result values obtained under turbulent flow conditions	58
Table 4.3.	Signal to noise ratio for laminar flow	59
Table 4.4.	Signal to noise ratio for turbulent flow	59
Table 4.5.	S/N ratios and weight factors according to factor levels of laminar results	60
Table 4.6.	S/N ratios and weight factors according to factor levels of turbulent results	61
Table 4.7.	ANOVA results for laminar flow and contribution ratios for results	62
Table 4.8.	ANOVA results for turbulent flow and contribution ratios for results	63
Table 4.9.	Normalization and Gray Relational Grade Calculation according to laminar flow results ……..	64
Table 4.10.	Normalization and Gray Relational Grade Calculation according to laminar flow results ……..	65

1. INTRODUCTION

Since the industrial revolution, the population density has increased gradually, and consumption has also increased in parallel. The increase in consumption in all sectors has led to its increasing importance in logistics and the use of vehicles with internal combustion engines such as trucks, commercial cars, motorcycles, planes, etc. more frequently. Due to this increase, carbon emissions have increased and have a negative but significant effect on climate change (Wrigley 2013) . Various steps have been taken to keep climate change under control and to reduce it to the pre-industrial levels within a certain period of time, and decisions have been taken and implemented by countries. The most comprehensive agreement currently in force is the Paris Agreement. According to this agreement, the use of vehicles with internal combustion engines will be restricted and alternatives such as electric vehicles will be provided to replace them. For this reason, large investments and incentives are made by countries and institutions for the development of electric vehicles and its technologies.

The prevalence of electric vehicles depends on various factors. The first of these is the incentives made to the buyer. With these incentives, it is aimed to minimize the price difference between vehicles with combustion engines and electric vehicles for the consumers. A second reason is the comfort criteria for the cabin, which includes the heating and cooling features of the cabin. Unlike fuel-powered vehicles, the fact that the amount of residual heat is not high in electric vehicles means extra energy will be spent for heating and cooling systems. This shortens the range and causes more frequent battery charging breaks. Another and one of the most important reasons are the concept called range anxiety. This concept indicates the anxiety experienced by the users when they cannot predict whether the current vehicle, they drive can go the way they want to travel. This is of great importance in the car selection decisions of the consumers.

The effective use of heating and cooling systems that have been used for years in ICEVs, increasing the vehicle range, and shortening the charging times are important factors in the selection stage of electric vehicles from the customer perspectives. These expectations showed the necessity of developing battery systems. However, the development of battery

systems and the addition of fast charging features have brought along heating problems that may occur in the battery during charge and discharge mode. For this reason, studies on battery cooling systems are carried out by companies and institutions around the world. Since the batteries are electrochemical systems and they are designed to achieve the highest efficiency at their optimal temperatures, the temperature and humidity of the environment are the key elements that directly and notably affect their performance, state of health (SOH), charge acceptance and cycle life. When they work in environments with temperatures outside these optimum temperature values, they may cause negative and critical consequences such as stopping the operation, melting, damaging the vehicle, creating flames or emitting dangerous gases. Studies have shown that when lithium-ion batteries are used in extreme conditions for a long period of time, their state of health values are decreases sharply (Friesen et.al 2016).

This sensitivity of lithium-ion batteries to the temperature necessitates the use of additional systems. These systems are called battery thermal management systems (BTMS) in general. The main purpose of using these systems is to maintain the temperature of the battery in the operating temperature range within a uniformity, to prevent possible damage to the battery and to ensure that the battery works with its maximum efficiency.

The selection of the cooling system technology of the batteries varies depending on the geometry of the battery, its location in the vehicle, the size and material of the area to be cooled. These systems are basically classified as air cooling, liquid cooling and phase change material (PCM). Air cooling solutions are the cheapest and simplest of these systems, but these solutions should be used in non-critical cases because the control of the temperature and uniformity are more difficult to than other systems. Solutions containing liquid cooling are used when a more uniform and effective cooling is required. One of the disadvantages of this system is that it is heavier than systems with air cooling. Finally, PCMs are materials that generally rely on solid-liquid phase transitions during temperature changes. The existing material changes state and turns into a liquid when the heat is absorbed and vice versa (Sundén 2019).

In this study, the liquid cooling plate for the lithium-ion battery used in the G6 vehicle produced by GOUPIL Industries was designed, optimized and its effect on cooling was investigated. CREO software was used in the design of the plate. The heat flux value required for the main analysis was provided with the existing battery whose generic model was made with the AMESIM software. This 1D model has been validated by charging tests. Finally, the designed cold plate was analyzed by using ANSYS Fluent. The aim of the carried-out study is to optimize the conditions that provide the best and the most uniform thermal performance and the most optimal pressure loss with the liquid cooling plate application used to remove the excess heat from the battery.

The theoretical basics and the resources of the research, which constitute the second part of the thesis, contain general information about lithium-ion battery and cooling systems, and the studies done so far are examined. In the third chapter, under the title of material and method, the equations used in the thesis, the model of the study and the boundary conditions are presented. The results of the analyzes are included in the fourth chapter, which is the findings and discussion. Finally, all the results are shown in the fifth section under the results.

2. THEORETICAL BASICS and LITERATURE REVIEW

General Background

In this section, information that will contribute to the research and help to better understand the subject is given. The transition phases of vehicles with internal combustion engines to electric vehicles, the environmental effects of electric vehicles andthe decisions taken on this subject are mentioned. Apart from their environmental impacts a short summary has been made about the future of electric vehicles.

Ansys Fluent and Amesim Software

In parallel with the advancement of technology, the increase in needs and therefore the increase in the demand for consumption has led to the growth of sectors that include transportation technologies such as cargo and passenger transportation. For this reason, time has become an important factor in the competition of these rapidly growing sectors with their competitors in the global market. Since product development and system improvement stages and prototype creation are very costly and time-consuming, the development and use of specific software that will shorten this time and minimize the number of prototypes is increasing.

Ansys Fluent is a fluid simulation software known for its advanced physical modeling capabilities needed to model flow, turbulence, heat transfer and chemical reactions.
Simcenter Amesim is a software that enables users to model, analyze and optimize multi-physical systems. Since it has various libraries and sub elements for fluid, electrical, automotive, thermal and propulsion systems it provides freedom in systems that can be modeled while reducing development cost and time.

In this study, the lithium-ion battery used in the Goupil G6 vehicle was modeled using Amesim 2021.2 and a validation study was carried out for the heat flux value required for limit conditions. By optimizing the existing model, realistic results were obtained. Thus, the systems created can be accepted as the base model and allow further studies with the

desired modifications. Furthermore, a liquid cooling plate was designed based on the battery used in Goupil G6 and analyzed using ANSYS FLUENT 2021R2 software.

Environmental Background

Since the industrial revolution affected human life in many ways, it is considered a turning point in the history of humanity. With the industrial revolution, urbanization became widespread, average incomes and health opportunities increased, and accordingly, the population showed an unpredictable continuous growth. (Wilde 2021).

Industrialization and the growth of the population increased the demand for goods and caused the production volume and carbon-dioxide emissions to expand in direct proportion. According to the researches carried out, the carbon emission occurring in the last thirty years is more than the carbon emission between 1750-1990 (Ritchie 2019). The recovery of the economy after the Covid-19 pandemic and the increase in gas prices have led to a tendency towards non-renewable energy sources such as coal and carbon emissions to be higher than all values up to 2021 with 36.3 billion tonnes (“IEA” 2022).

Greenhouse gases (GHG) are various gases in the atmosphere that absorb infrared radiation and reflect it back to the earth which cause warm the planet (Kweku et al. 2018). Methane, water vapor, carbon dioxide, nitrous oxide, surface-level ozone can be shown as examples of these gases (Mann 2022). The degree of influence of these gases is determined by examining them in two different categories. The first of these is the life span in the atmosphere. Carbon dioxide is the most complexly removed gas because more than one process is involved. 50% of carbon dioxide is removed from the atmosphere in the first thirty years, 30% in several centuries and the remaining 20% in many thousands of years (Moore 2008, Anonymous 2012). Methane is mostly removed from the atmosphere by chemical reactions and this process takes only about 12 years and 109 years for nitrous oxide (Anonymous 2012). The second characteristic feature used to determine the effect of gases in the atmosphere on greenhouse effects is their ability to absorb and reflect energy. By examining these two characteristics, a generic scale for measuring the effects called Global Warming Potential (GWP) is created. According to

this scale, the GWP value of CO_2 in 100 years is 1, while the value of methane is 28 and N_2O value is 265 (Myhre et al. 2013). However, although the GWP value of carbon-dioxide is the lowest among the others, the amount and the lifetime of CO_2 is the highest among mentioned gasses ("Anonymous" 2017). For this reason, the most important and dominant greenhouse gas is carbon-dioxide.

CO_2 is produced both naturally and by human activities. However, it is the gases that are harmful to the nature are the result of human activities, such as burning fossil fuels, deforestation, that cause the greenhouse effect. In Figure 2.1, the percentage of carbon-dioxide production depending on the sectors is shown. According to the study conducted in 2020, the transportation and the electric power generation sector has the highest carbon dioxide emission with 25%. It has been observed that carbon emissions from buildings account for one-fifth of total emissions. The remaining sectors have a total value of 30%. The importance of the role of only three main sectors, which are electric power, transportation, and buildings sectors, in reducing carbon emissions is very clear.

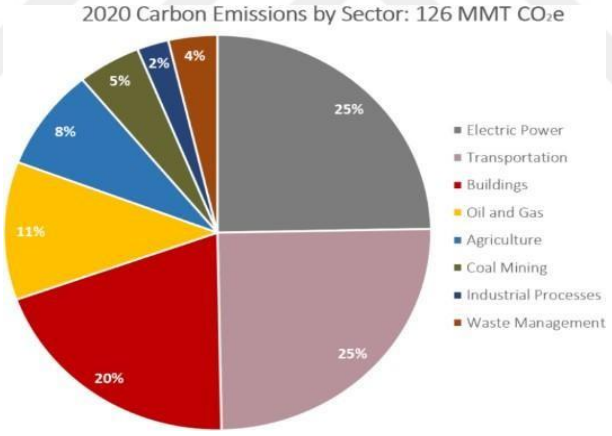


Figure 2.1. Percentage of CO_2 production depending on the sectors ("Anonymous" 2020)

As claimed by another recent study on carbon-dioxide emissions in the transportation sector, the image of which is given in Figure 2.2, it has been observed that passenger cars and trucks constitute 41% and 22%, respectively, in the transportation sector. The most of this carbon-dioxide emission in transportation is caused by road transportation because most of the existing vehicles work with internal combustion engines. These areas are

followed by shipping with 11% and aviation with 8%. Rail, two/three wheelers, buses and light commercial vehicles make up the remaining 18%.

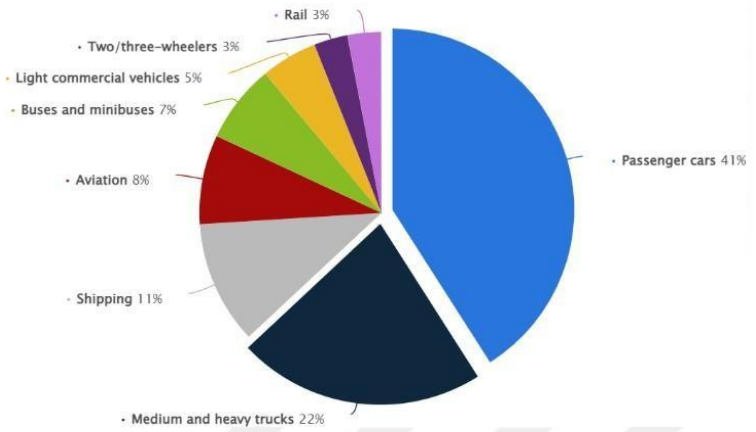


Figure 2.2. CO_2 emissions in the transportation sector ("Anonymous" 2021 May)

Due to such an increase in carbon emissions, it has been recorded that the world has warmed by 1.1°C since 1990. Although this seems like a low value for now, it is an ascension that should be taken seriously for the future. In consequence, companies, municipalities and countries take various precautions against global warming. One of the most important cautions in force to reduce global warming is the Paris agreement, which was signed by various countries in 2016. The aim of this agreement is to reduce the current warming below 2°C and above pre-industrial levels, preferably to 1.5°C in long term (Maizland 2022). In the same agreement, it was stated that 50% of carbon emissionsshould be cut by 2030 in order to keep global warming below 1.5°C (UNFCCC 2015).

Within the scope of the improvements made to achieve the targets, different scenarios are created, warming predictions for the future are made and it is checked whether they match the desired goals. These scenarios are as seen in Figure 2.3. The first scenario, shown in pink, is the prediction for a situation where no policy is applied to keep global warming at a certain level. As it is seen, if carbon emission continues in this way without any improvement, it is expected that the earth will warm up between 4.1°C and 4.8°C by the year 2100. The scenario indicated in orange is the expected value at the end of 2100 with the current policies. It is clear that even with current policies, global warming is expected to rise to a value between 2.5°C and 2.9°C unless more steps are taken to reduce

greenhouse gas emissions. If all countries fulfill their commitments, this value will remain at 2.1°C, but sharp reductions should be made in emissions until 2045 for below 2°C and until 2027 for 1.5°C (Ritchie, H., et al. 2020 August).

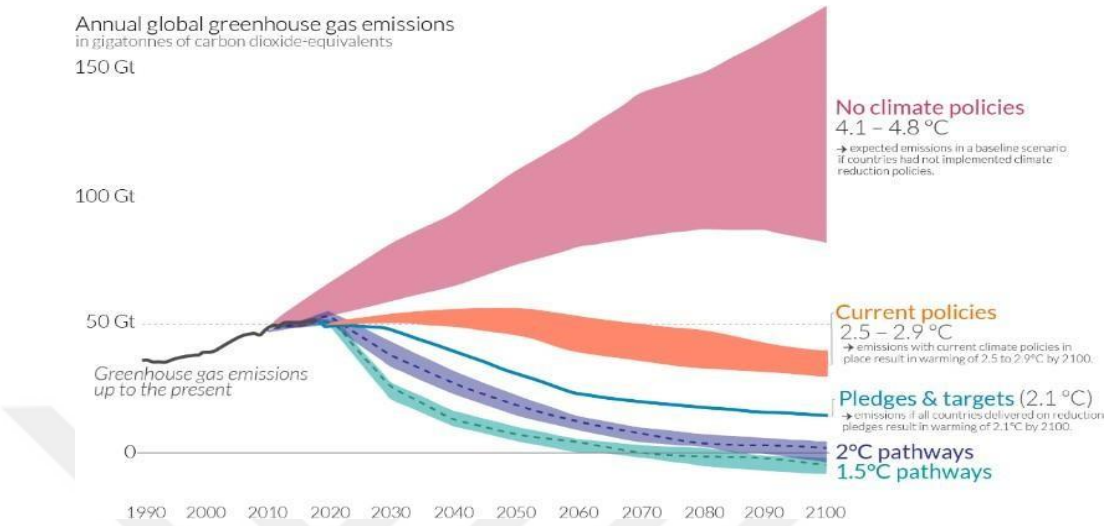


Figure 2.3. GHG emissions and warming scenarios (Ritchie, H. et al. 2020 August)

One of the most important goals of the countries is to reach net zero emissions by 2050 and to keep the global warming value at 1.5°C by the end of 2100 (Rogelj et al. 2015, IEA 2022 December). However, to close the gap between rhetoric and reality, it is necessary to take aggressive actions immediately. Although the pathways necessary to reach these goals have been determined by various committees, there is no general rule that fits all countries. For this reason, countries should make their own improvements within the framework of the above-mentioned targets according to their country dynamics. However, it is vital to focus on the first three main sectors seen in Figure 2.1 in order for the measures to be taken to be effective regardless of the country. One of these sectors is the transportation sector. The biggest cause of carbon emissions in this portion is the internal combustion engines used in transportation vehicles. Instead of these engines, which use carbon-based non-renewable fuels to work, the use of electrically powered engines is encouraged.

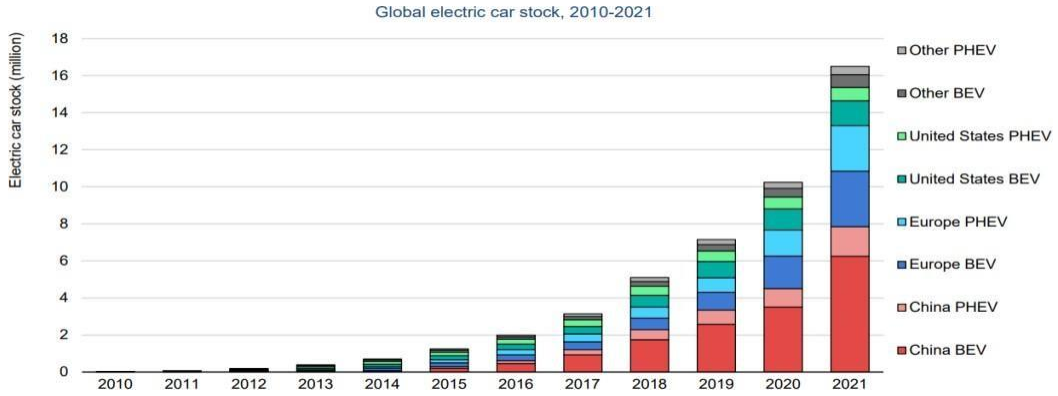


Figure 2.4. Regional rates of BEV and PHEV between 2010 to 2021 (IEA, 2022 May)

Figure 2.4 indicates the regional rates of BEV and PHEVs between the years 2010 and 2021. Throughout the research, it was found that the total amount of electric vehicle sales in 2012 was reached in just one week in 2021 (IEA, 2022 May) and by 2021, the number of electric vehicles actively used increased to 16.5 million. Although the current sales cover 9% of the global market, the fact that it has four times the volume of the sales values for the year 2019 alone highlights the rapid increase in sales trends. When the number of electric vehicles on the roads is examined on the basis of countries, China takes the first place with a total of 8 million units. It is seen that the countries with the second highest volume in the global market are the countries in Europe. When analyzed by country, Norway comes first with 86%, followed by Iceland with 72%, Sweden 43%, Netherlands 30% and France 19% (IEA, 2022 May). Although the USA doubled its sales in 2020, it only accounts for 10% of the global market.

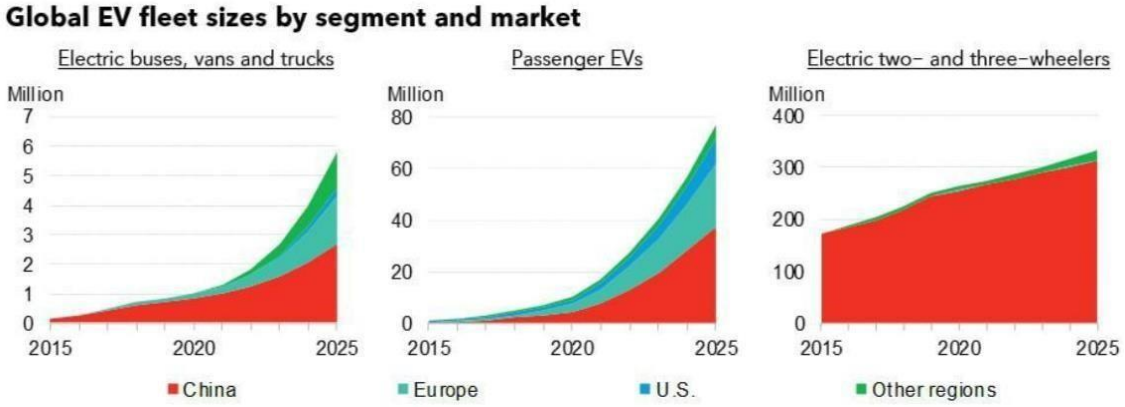


Figure 2.5. Global EV fleet size predictions ("BloombergNEF", 2022)

According to the report by Bloomberg NEF, which can be seen in Figure 2.5, the sales of passenger electric vehicles, which were 6.6 million in 2021, are predicted to reach 20.6 million by 2025. While China and Europe account for 80% of these sales, it is estimated that the USA will make up the remaining 15%. Despite the increase in EV sales, it is expected that ICEVs will also increase until 2024 but will go a downward trend after this year. It has been stated that the sales of heavy-duty trucks powered by electric motors, of which a total of ten thousand were sold in 2021, increase between 35% and 60% each year and will be fully electric by 2030.

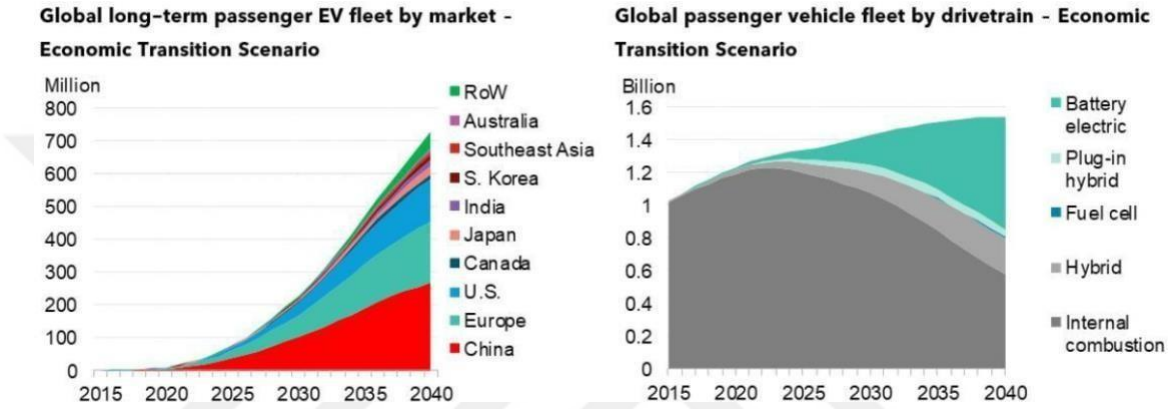


Figure 2.6. Fleet predictions by countries according to ETS ("BloombergNEF", 2022)

Although the sales of electrically powered vehicles have increased, this rate of increase is not the same all over the world. Long-term passenger EV fleet numbers and drivetrain distributions are given in Figure 2.6. In these estimates for 2040, China, Europe and the US have the highest percentages of EVs. It is seen that the electric vehicle usage rates in countries such as India, Mexico, Turkey, Russia and Brazil, where the economy is not stable, support policies are limited, are very low compared to the world. When the distribution estimates in drivetrain types are examined, it is seen that the sales of vehicles with internal combustion engines will increase between 2020-2025, but then decrease with the increase in sales of battery electric vehicles. It is predicted that plug-in hybrid vehicles will also enter a decreasing trend as of 2025, because of the increasing oil prices and cost-effective, improved batteries.

Since electric vehicles do not work with carbon-based fuels, they do not emit any carbon during their use, therefore they are also called zero-emission vehicles. Although they do not emit carbon while driving, their carbon footprints are not zero because they contribute to carbon emissions during their production (Moseman 2022).

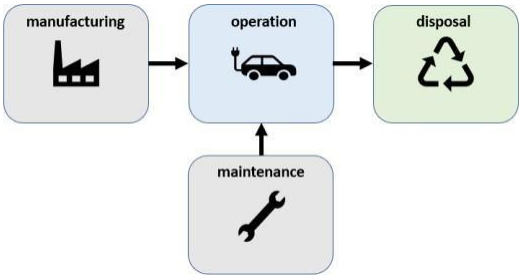


Figure 2.7. Life cycle of an electric vehicle

Although the vehicle's propulsion system is the first thing to look at when comparing the carbon emissions of the vehicles, it is more appropriate to make a life-cycle assessment for a correct comparison. The life cycle of every vehicle produced generally includes the production of the vehicle, the source of the energy used, its operation and its recycling, which can be seen in Figure 2.7 (Wu et al. 2018). Considering vehicles powered by electric motors, it is known that the main carbon emissions are not during usage such as vehicles with internal combustion engines, but during the production of energy storage systems and drivetrains.

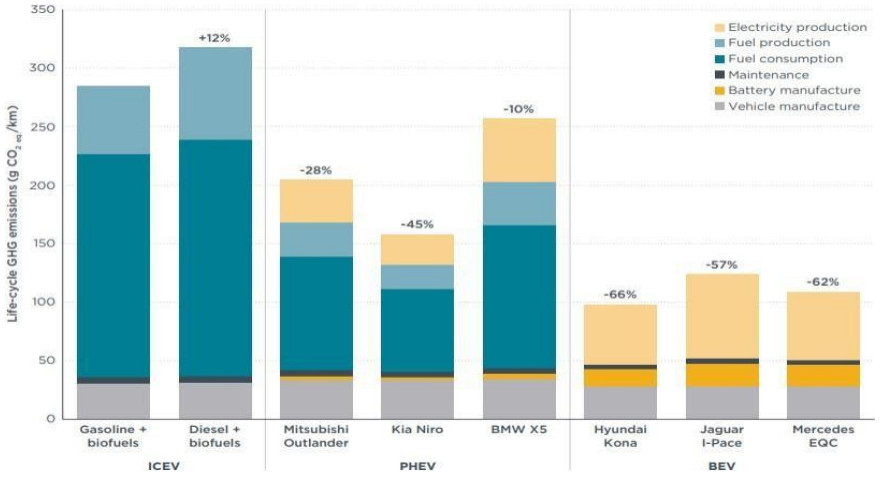


Figure 2.8. Percentage of carbon emissions produced by ICEV, PHEV and BEVs during their life cycle (Bieker, G., et al. 2022 March)

In Figure 2.8, the graph of a research made on the basis of Germany in March 2022 is given. In the study, the carbon values released during electricity production, fuel production, maintenance, battery production and production of ICEV, PHEV and BEV were compared. As can be seen from the figure, the carbon emissions that occur during production are almost equal for all vehicle types, regardless of the propulsion systems of the vehicles. When only ICEV is examined, it is seen that the highest carbon emission occurs during fuel production and fuel consumption. In terms of fuel, vehicles working with diesel cause 12% more carbon emissions than those working with gasoline. When PHEVs containing both an electric motor and an internal combustion engine are examined, it is seen that the most effective area in carbon emission is fuel consumption with non-renewable energy sources. Although they have an internal combustion engine, it has been found that thanks to electric mode, they emit 10% to 45% less carbon compared to vehicles with only internal combustion engines. Considering other reasons, while the carbon released during electricity production comes in the second place and fuel production also constitutes the third largest segment. Finally, the carbon emissions of vehicles with only electric motors are listed according to their causes. It has been observed that a large part of the carbon emissions of fully electric vehicles is due to the mode of production of the electricity used. This is followed by the percentage of carbon released during battery production. It has been determined that these vehicles emit between 42% and 66% less carbon compared to vehicles running on completely non- renewable fuels, such as gasoline.

In general, it is known that vehicles with fully electric motor emit less carbon emissions than those with internal combustion engines. However, the extent to which electric vehicles emit carbon varies from country to country. The level of these emissions varies according to the method used in electricity generation.

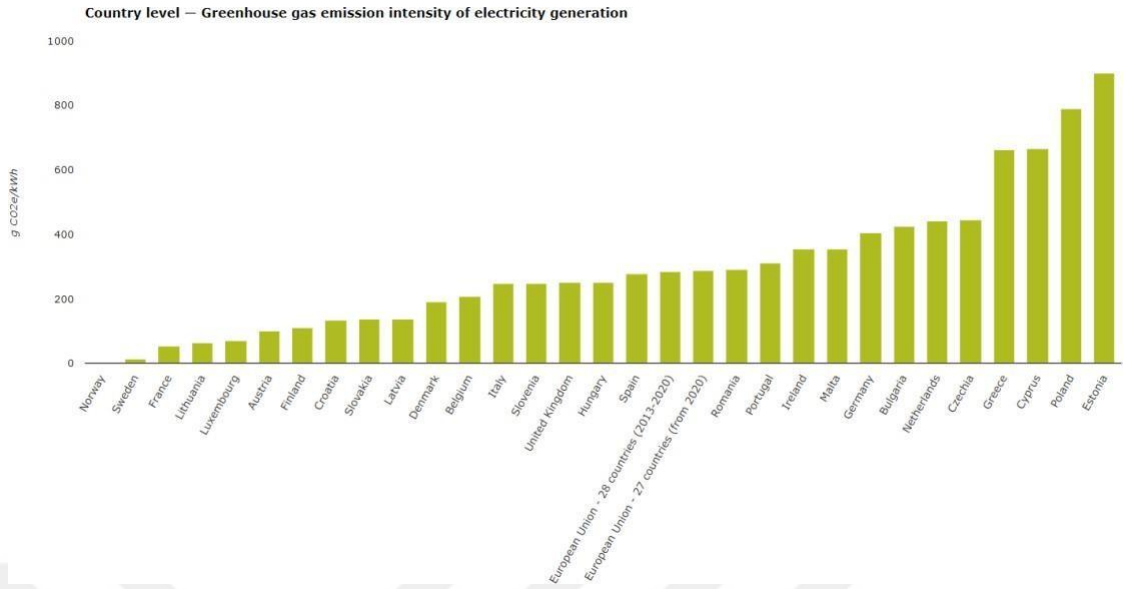


Figure 2.9. Distribution of GHG emissions by European countries ("EEA" 2022 October)

Electric vehicles can be charged with electrical energy produced using various primary energy sources such as gas, oil, solar, wind, and nuclear. Therefore, GHG emissions values will also be different depending on these primary sources. In Figure 2.9, the distribution of GHG emissions by countries in Europe is given. When the graph is examined, it is seen that the lowest value is in Norway and Sweden, which use electricity produced from renewable energy sources. France is in the third place, which uses mostly nuclear and renewable energy sources. Poland and Estonia are among the countries with the highest GHG emissions because of the high consumption of coal used for electricity generation.

In line with the information given, it is seen that the use of electric vehicles should be expanded since they do not emit carbon emissions during their use in line with the "net zero" targeted for 2050. However, although the amount of carbon released during the usage period is important, necessary precautions should be taken by considering the amount of carbon that will be released during the production, logistics, maintenance and recycling of these vehicles.

Theoretical Background

In this section, detailed information about the lithium-ion battery, its working principle and cooling systems are given.

Lithium-ion Battery

Lithium-ion batteries are the devices that convert chemical energy into electrical energy, store it and release this energy when needed. It contains an anode, cathode, separator, electrolyte and two current collectors (positive and negative) which can be seen in Figure 2.10. The negative electrode of the cell is called the anode, and the positive electrode is called the cathode. The separator is an important safety element that separates the anode and cathode from each other, allows the passage of lithium ions during charge and discharge but prevents possible short circuits by not conducting electricity. Lastly, electrolyte is a gel or liquid element in the battery that helps transfer lithium ions from anode to cathode.

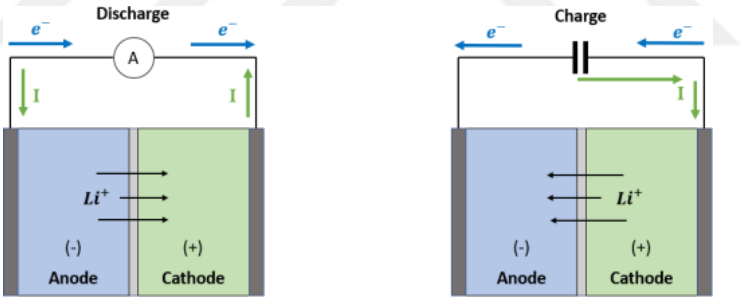


Figure 2.10. Schematic representation of the working principle of lithium-ion battery

During the charging process, the lithium ions tend to move from cathode part to anode part of the cell through the electrolyte. The more ions placed on the anode part consisting of layers, the greater the voltage between the negative and positive electrode. This movement of lithium-ions causes free electrons to increase in the anode part, which creates a charge in the positive current collector. In the case of discharge, these ions embedded between the layers are released and transferred to the cathode. The more

lithium ions move to the positive side, the more discharge capacity occurs (Woodford 2022).

The usage areas of lithium-ion batteries are quite wide, and the capacity required for each area is not the same. For this reason, batteries containing different chemicals compatible with different sectors, such as automobiles and household appliances, have been produced. Information including different battery types can be as seen in Table 2.1.

Table 2.1. Types of li-ion battery (Battery University, 2014)

Chemical Name	Material	Short Form	Information
Lithium Cobalt Oxide	LiCoO2	Li - cobalt	High specific energy Short battery life Cell phones, laptops, electronic cameras
Lithium Manganese Oxide	LiMn2O4	Li - manganese	High temperature stability Safe Medical equipment and devices, electric vehicles
Lithium Iron Phosphate	LiFePO4	LFP	Durability and long lifecycle Thermally stable and safe Electric vehicles and bikes
Lithium Nickel Manganese Cobalt Oxide	LiNiMnCoO2	NMC	High specific energy Low cost Low heating rate Electric vehicles
Lithium Nickel Cobalt Aluminum Oxide	LiNiCoAlO2	NCA	High energy with long lifespan Less safe than other Li-ion batteries Electric vehicles
Lithium titanate	Li4Ti5O12	Li - titanate	Extremely rapid recharge time Less efficient Aerospace applications and energy storage technologies in the future

The most important advantage of these rechargeable batteries is their high energy density. This means that three to four times more energy per unit mass can be store than other rechargeable batteries. The other advantages are the low self-discharge, quick recharge ability and longer life span. But there are disadvantages as well as advantages. The first thing that comes to mind is the decrease in the charging capacity over time due to loss of the lithium-ions during the charge and discharge. Another disadvantage is that it is very sensitive to temperature. When it is operated at an ambient temperature different from the nominal operating temperature, it causes both the capacity to drop considerably and the battery to have a negative effect on health (Matthe et al. 2011). For this reason, thermal management systems are often needed (Zubi et al. 2018).

Battery Thermal Management Systems

Batteries are highly affected by both hot and cold climates (Jaguemont et. al. 2016, Erdinc et al. 2009). It is known that at low temperatures, performance decreases, charge acceptance worsens, lifespan and energy capacity decrease (Ma et al. 2018, Wu et al. 2019). At high temperatures, it causes irreversible capacity and performance drops, as well as the formation of catastrophic thermal runaways (Ma et al. 2018, Wu et al. 2019). It is necessary to use various systems in order to keep the performance and life span at the optimum and to prevent the thermal runaway and to eliminate the elements that threaten the safety of the battery (Chombo & Laoonual 2020). Battery thermal management systems are safety components used to control both the heat produced by the battery and the effect from the environment so that the battery works in the optimumtemperature range (Park & Jung 2013).

These systems can be examined under two general headings as passive and active. Subcategories of these systems can be divided into air cooling, liquid cooling, and phase change material (PCM) cooling.

Air Cooling

These systems are systems that use the cabin or outdoor air as a cooler. These systems are frequently used in many industries due to their low cost, simple structure and easy repairability. However, since the air has a lower heat capacity and low thermal conductivity, it cannot provide effective cooling (Park & Jung 2013). Toyota Prius and Nissan Leaf can be shown as examples of the most well-known electric vehicles using this technology (Wu et al. 2019).

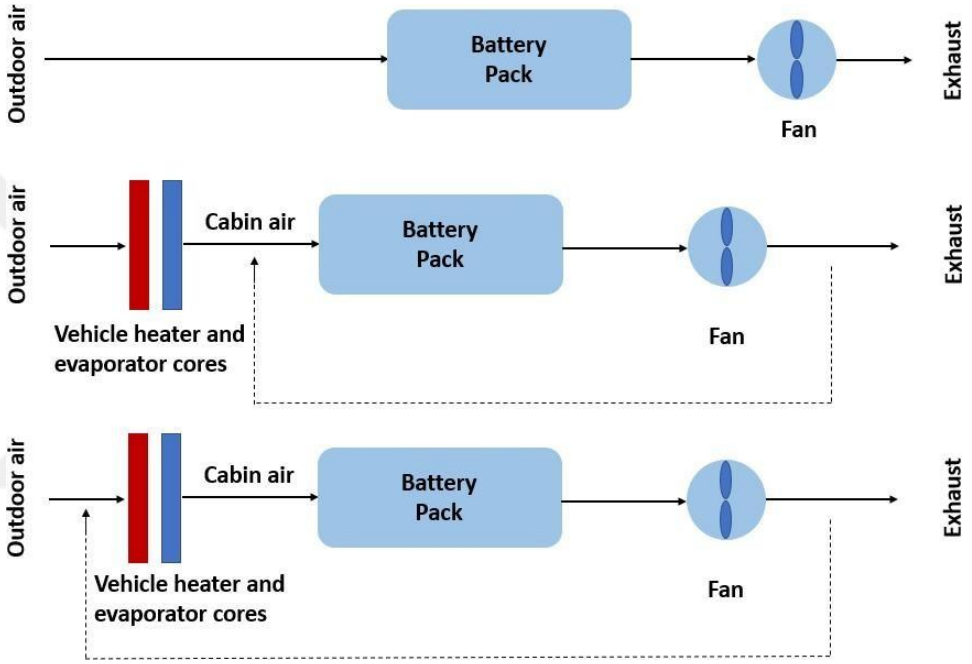


Figure 2.11. Active and passive air cooling (Pesaran 2001, Kurmaev et al. 2020)

Cooling can be provided by natural convection (passive) or by forced convection (active). However, natural convection is only suitable for low density batteries. A sematic representation of passive and active air-cooling systems is given in Figure 2.11. While the passive systems seen in the first schematic system in the figure take the air directly from the atmosphere or the cabin, the active systems, which are the other systems in the figure, take the preconditioned air from a heater or air conditioner (Park & Jung 2013). While the system is being designed, it should be kept in mind that the temperature in themiddle zone and the output zone of the battery will be higher than in the other zones, andthe necessary arrangements should be created accordingly.

Liquid Cooling

These are systems in which liquids are used as a coolant. They have higher heat removal rates due to their higher density and heat capacity compared to air. For this reason, they are frequently used in electric vehicles. In general, there are three different systems, namely immersing cooling, direct cooling, and indirect cooling. In immersing cooling, the battery modules are directly in the dielectric liquid. In direct cooling, the battery surface is in contact with the refrigerant. It is not used in electric vehicle batteries due to its impracticality and safety reasons. On the other hand, indirect cooling is a very common cooling system in vehicles, using a cooling plate or jacket. Indirect cooling is very simple compared to other systems, and higher flow rate is obtained because the viscosity of the refrigerant liquids used is lower than that of dielectric liquids.

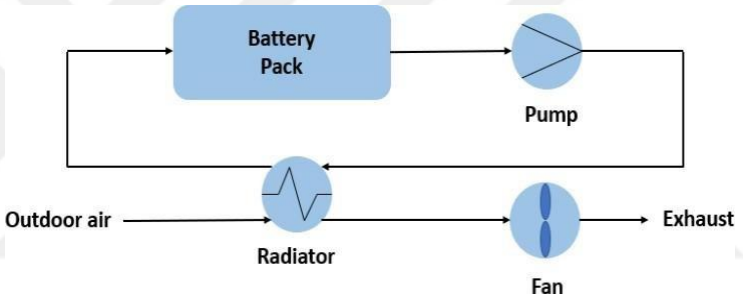


Figure 2.12. Passive liquid cooling system (Pesaran 2001, Kurmaev et al. 2020)

Figure 2.12 presents the sematic scheme of passive liquid cooling. The coolant is circulated in a closed system with the help of a pump. The heat in the battery is absorbed by the liquid circulating in the system and this heat is released through a radiator. The cooling power depends on the temperature between the ambient air and the battery. Although the fans behind the radiator improve cooling performance, the passive fluid system can become useless if the ambient air is higher than the battery temperature or the difference is too small.

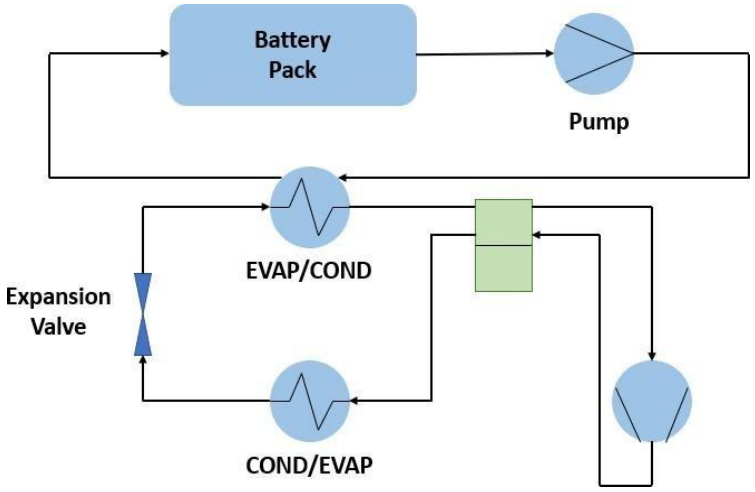


Figure 2.13. Active liquid cooling system (Kurmaev et al. 2020)

The systematic scheme of an active liquid cooling system can be seen in figure 2.13. In these systems, there are two different loops, the primary loop, which is similar to the loop in the passive system, and the secondary loop, which is simply the air conditioning loop. In this system, the cooling liquid coming from the battery is transmitted to the evaporator with the help of a pump and connects it to the second loop required for cooling. In cases where it is desired to heat the battery, this element acts as a condenser, while the other heat exchanger acts as an evaporator.

2.2.2.3. PCM Cooling

A phase change material (PCM) is a material that releases/absorbs energy at the phase transition to be used to provide useful heat or cooling and to control temperature fluctuations (Wu et al. 2019). A significant amount of heat energy is absorbed or released during the phase transition of a material. In PCMs, it is tried to control the temperature by taking advantage of this phenomenon. PCM is mostly used in combination with air cooling systems.

2.3. Previous Studies

Due to climate change, various regulations have been brought to the transportation sector and therefore investments in electric vehicle technologies have increased. Battery and cooling systems have become the most important of these technologies. Because of the high energy density and low self-discharge, the demand for lithium-ion batteries is expected to increase by 18.1% by the end of 2030 (“Anonymous” 2019-2020). Although it is a battery with many advantages, it is highly sensitive to temperature. Since the electrolyte inside the battery cell is flammable, the battery should be used and charged in certain temperatures. This obstacle limits the developments in battery technology and manufacturers are looking for various solutions to safety problems caused by overheating. Liquid cooling is one of the systems used to cool the battery.

A liquid cooling system with changing surface which is between the channels and cells is design by Shang et al. (2018 October) and it is analyzed with different mass flow rate, inlet temperature and width of cooling channel dimension to observe the performance and the consumption of the pump. Increasing the inlet mass flow rate was effective in decreasing the maximum temperature, but it did not enhance the uniformity of the temperature between cells. In terms of inlet temperature of the coolant and the width of the cooling channel, it has been seen that the temperature of the battery is proportional to the temperature of the inlet and inversely proportional to the width size of plate. After examining these differentiators one by one, single factor analysis and orthogonal test were applied and optimization study was carried out for all the factors. Uniformity is ensured after optimization and the energy used by the pump is reduced.

Deng et al. (2019 July) studied the thermal performance of the lithium-ion battery using a cold plate. The study analyzed the effect of mass flow rate, number of cold plates, channel distribution and the direction of cooling into the temperature distribution. It has been found that the best cooling is provided by the design with more channels in the middle of the coil and the coolant flow direction affects the uniformity.

Ye et al. (2019 February) designed and optimized a cooling plate for a lithium iron phosphate battery. The orthogonal experimental design method is applied to the thermal model to optimize battery gap, the cross-section dimension, and the cooling channel number of the plate. After the optimization of the plate, the difference between the maximum and minimum temperature decreased by 9.5%, while the pressure drop showed a decrease of approximately 17%.

Deng et al. (2018 June) published a review on the cooling performance of lithium-ion batteries with different coolants, design of battery packs and cooling strategies. In terms of coolants, a comparison was made between water, oil and additional nanoparticles. It has been determined that the most effective way for battery life and performance is liquid cooling. The configurations which are series, parallel and series-parallel studied for the battery pack design. Finally, information about active and passive, internal and external, direct and indirect cooling systems is given and examined.

Kim and Jarret (2013 July) worked on the impacts of operating conditions on the optimum design of cooling plate of battery of the electric vehicles. Temperature homogeneity, average temperature and pressure drop were considered while doing the measurements. With the change of operating conditions, the temperature homogeneity among the cells effected the most. The cooling plate is subjected to constant heat flux and optimized.

Panchal et al. (2020 April) developed a turbulence model of a cold plate with micro-channels and water coolant for batteries used in electric vehicles with a reverse engineering approach. The numerical operation was tested under different temperatures and for two different C-rates, which is 3C and 4C.

Chaab and Wei (2019 August) developed and experimentally analyzed a hybrid cooling system for the electric vehicle batteries. Since the system uses the capillary effect as the driving force of the coolant, no additional power is used. At the end of the study, the existing system improved both the cooling efficiency and temperature uniformity by 70% compared to the battery without any cooling solution. Compared with the air-cooled system, this improvement was found to be 20% for efficiency, 56% for uniformity.

A water cooled mini-channel plate for large sized prismatic lithium-ion battery designed and simulated by Panchal et al. (2017 May). The experimental and numerical simulations were performed with different discharge rates and operating temperatures. It was observed that as the c-rate and operating temperature increased, the cooling plate temperature increased in parallel. In addition, it has been observed that the temperature sensors close to the anode and cathode is measured higher temperatures than the sensors located in the middle region of the battery surface.

Xu et al. (2019 December) utilized numerical study to optimize a cold plate splitter for lithium battery. Orthogonal experimental design method is used to optimize the splitter number, length, angle, the distance between two splitters and the offset distance. As the number of splitters increases, the mean temperature difference of each cell decreases. Additionally, the deflection angle and splitter length highly effected thermal performance of the battery pack.

Huo et al. (2014 October) investigated the influence of thermal management system of a battery by using cold plate with mini-channels. The temperature distribution in the discharged state of the battery is investigated in different number of channels, flow direction, inlet mass flow rate and ambient temperature cases. As the number of channels on the cooling plate and inlet mass flow rate increased, the maximum temperature reached in the battery pack is also decreased. It has been observed that the effect of flow direction is very less compared to the other parameters.

Turaka et al. (2021) compared different cooling systems for lithium-ion battery using CFD simulation. In the study, cooling plates with different configurations were modeled in three dimensions and analyzed using ANSYS under different mass flow rates. At the end of the simulation, pressure, velocity, heat transfer coefficient, mass flow rate and heat transfer rate for each geometry and inlet mass flow rate were printed as output. In the light of the analyzes carried out, it was determined that the calculated heat flux value in geometries with U-bend heat pipe in which RT50 is used as a phase change material is lower than the case which is used lithium-ion phosphate phase change materials. In geometries with straight channels, it was determined that the mass flow rate, heat transfer

rate and heat transfer coefficient value increased by increasing the inlet mass flow rate and heat transfer rate compared to bend type channels.

3. MATERIALS and METHODS

In this part of the thesis, the information about the necessary measures for the numerical solution of the investigated problem, the conservation equations used for the solution, the boundary conditions and the turbulence equations used for the turbulent flow are presented.

Validation Study

Since the geometries to be used in the thesis study cannot be validated experimentally, it is aimed to provide validation of the methods to be used during the analysis by considering a similar study. For the validation, the optimization of the heat sink used in electric vehicle batteries studied by Kim and Jarrett was chosen (Jarrett et al. 2011).

The chosen geometry for the validation study was obtained using the CREO software. The outer dimensions of the geometry are 1 [mm] x 160 [mm] x 200 [mm]. The geometry to be analysed is symmetrical, therefore the thickness is reduced to 0.5 [mm] and only half of the geometry was created in 3D. The cooling channel geometry with a width of 20 [mm] and a height of 0.75 [mm] was formed as 20 [mm] x 0.375 [mm] after halving it as specified in the paper.

Since the geometry contain both solid domain (plate) and fluid domain (cooling channel), both were created separately and assembled using CREO Parametric. After the creation of the geometry is finished, it is imported to the geometry part which can be found in the component systems in the ANSYS software. The imported geometry is as shown in Figure 3.1.

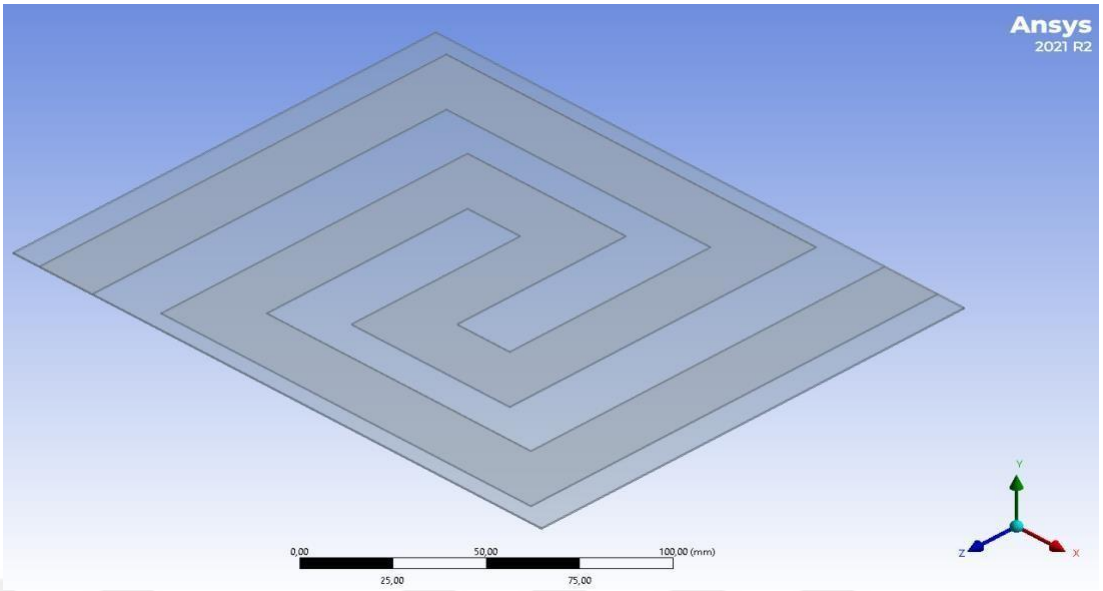


Figure 3.1. Validation geometry before slice operation

Since this geometry has two different domains, it was decided to mesh the fluid and solid domains separately. For this reason, the geometry is divided into rectangular volumes using the slice operator for convenience which can be seen in Figure 3.2. To create independent parts (for fluid and solid domains) within the model, not all the volumes in the geometry but only the volumes containing domains of the same type were created as a part. Thus, two different domains were saved as two different parts.

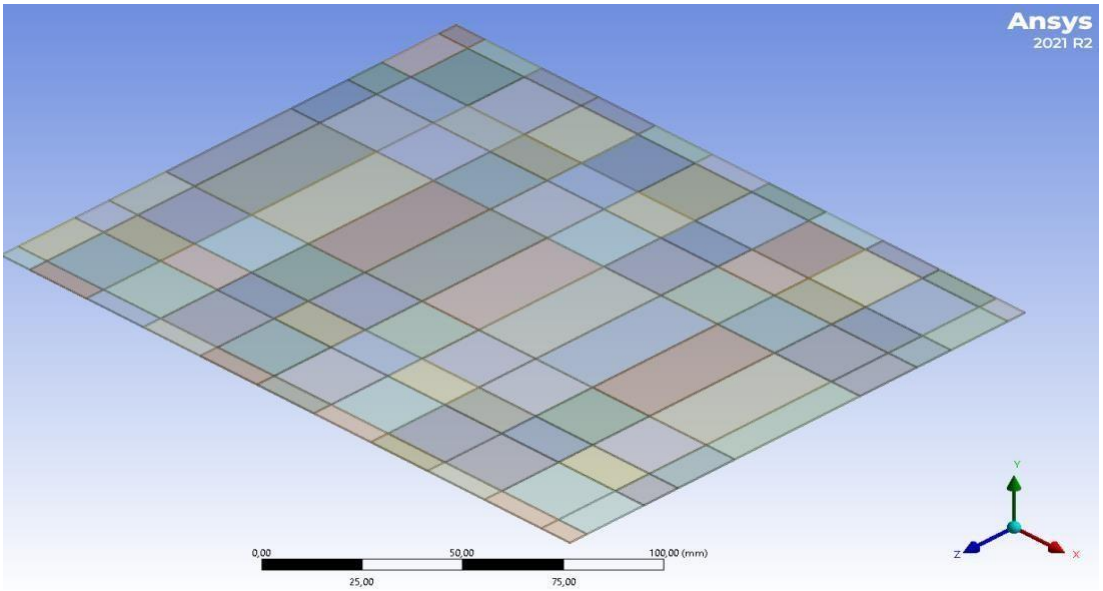


Figure 3.2. Validation geometry after slice operation

The created geometry is transferred to the mesh component in the component systems and physics preference is set to CFD. First, the default mesh was applied, and the mesh structures of the fluid and solid domains were arranged considering the obtained structure. Since the flow will take place in the fluid domain, the mesh structures are compacted in this region. The final state of the mesh structures can be seen in Figure 3.3 and the zoomed version of the region marked in red can be seen in Figure 3.4.

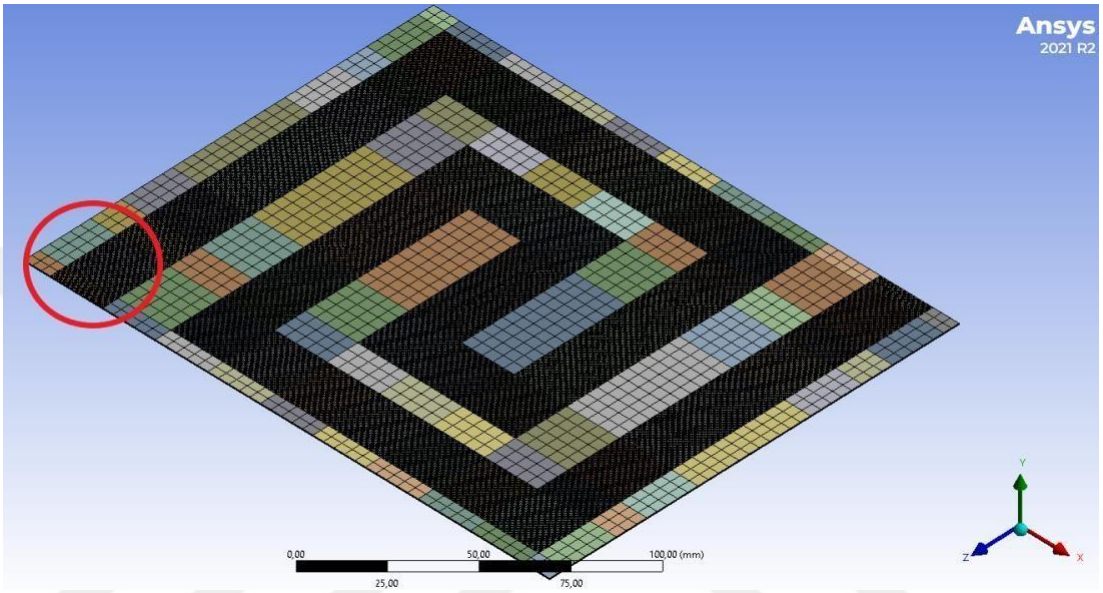


Figure 3.3. The mesh structure of the geometry

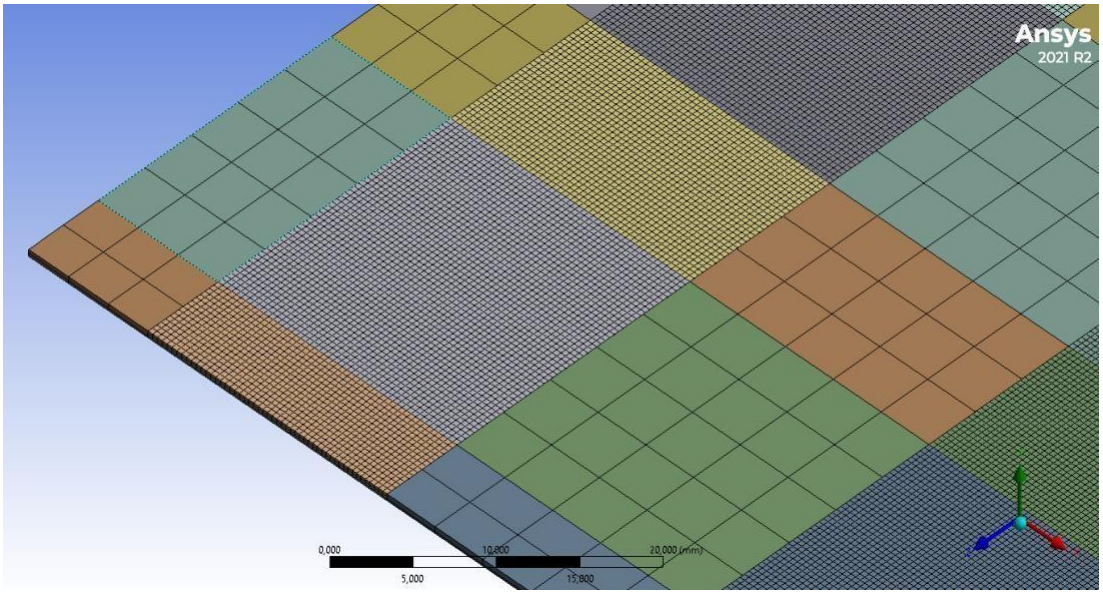


Figure 3.4. Detailed view of the mesh structure of the geometry

A total of 243 971 elements are used and 240 874 of them are in the fluid domain. The number of elements in the reference study was tried to be reached for the current mesh structure. Skewness is a quality indicator value that expresses the difference between shape of the cell and shape of the equilateral cell and expresses that the quality of the mesh structure gradually decreases as it approaches zero to one (ANSYS Meshing User's Guide 2013). The maximum value of skewness should be kept below 0.95 to avoid convergence difficulties. The average skewness is seen as 0.00246 and the maximum skewness is 0.54219 which is below the recommended level. Additionally, in terms of orthogonal quality, which is another indicator for the quality of the cells, the best cells have a value close to 1 and the worst cells will have a value close to 0. For this case, the average orthogonal quality is seen as 0.99942.

After the mesh quality was checked, the name selection was created to define the boundaries. For the first step, the fluid and solid volumes, the inlet-outlet, wall, symmetry, and heat flux surfaces seen in Figure 3.5 are named.

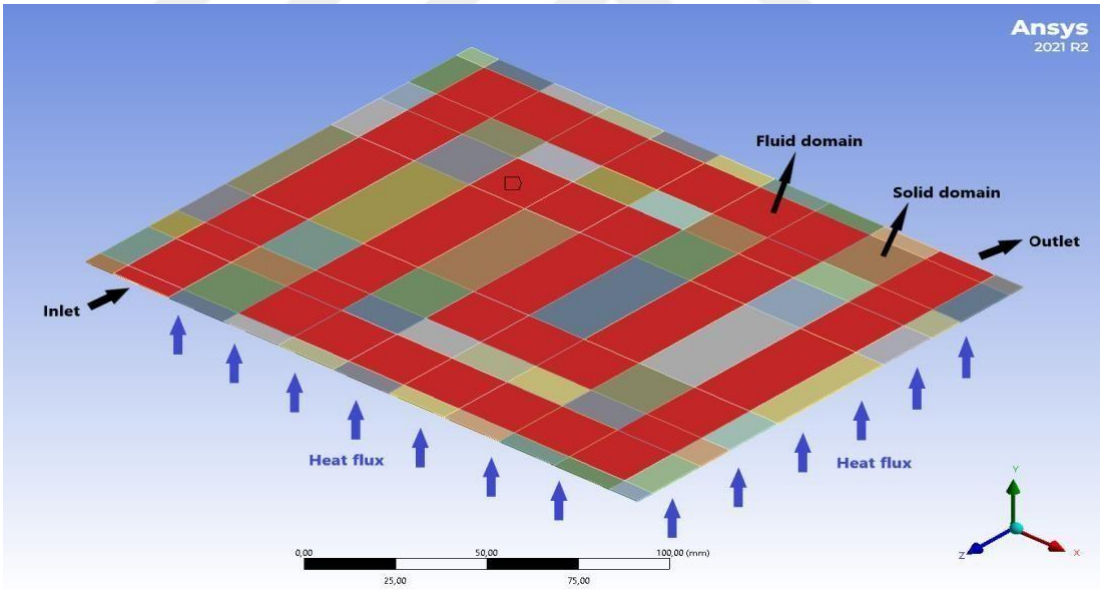


Figure 3.5. Name selection for validation study

In the second step of the name creation, the surfaces shared by fluid and solid domains are determined and named as interfaces. The reason for doing this is that both domains

are created separately while the geometry is being created. Otherwise, the problems involving heat transfer cannot be solved because two different domains cannot interact. After the names are defined, the created mesh structure is transferred to the fluent component. The final geometry and the inlet-outlet boundary conditions can be seen from Figure 3.6.

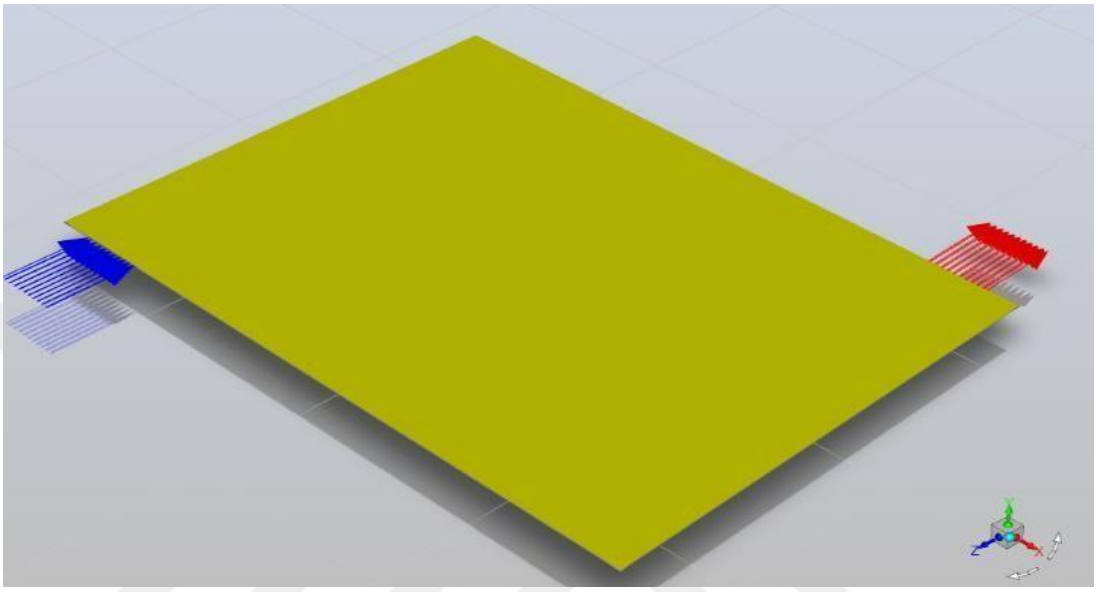


Figure 3.6. Imported validation geometry to the fluent component

The energy equations are turned on and the viscous model type is chosen as laminar. The fluid that passes through the fluid domain is water-ethylene glycol. Since it is not in the Fluent database, a new fluid has been created and added to the material part. After that, the new created fluid was introduced to the fluid domain in the cell zone condition. The solid domain is left in the default material, which is aluminum. Entries can be found in the table below.

Table 3.1. Coolant properties used in validation study

Coolant name:	Water-ethylene-glycol
Coolant density $[\boldsymbol{kg.m^{-3}}]$:	1065
Coolant specific heat* $[\boldsymbol{J.kg^{-1}K^{-1}}]$:	3494
Coolant conductivity $[\boldsymbol{W.m^{-1}K^{-1}}]$:	0.419
Coolant viscosity $[\boldsymbol{Pa.s}]$:	0.00315

*Property stated at 300 Kelvin.

Inlet boundary condition was set as mass-flow-inlet and 0.0005 (kg/s) value was given as input. Due to the current coordinate system, the flow direction is set to -1 in the z direction. The outlet condition is set to pressure-outlet. For the heat flux boundary condition 500 (W/m^2) is given. The interface-solid and interface-fluid surfaces created during the name selection are matched in the mesh interfaces section.

For the solution method, the scheme is selected as SIMPLE and flux type arrange as Rhie-Chow: momentum based. The calculation was started by leaving the relaxation values at their default values. Convergence criteria is set to 10^{-6} for the residuals. After hybrid initialization, calculation was run.

As stated in the report, three different printouts were taken and compared. They are;

- Mean temperature on the heat flux surface
- Standard deviation of temperature on the heat flux surface
- Area weighted average total pressure on the inlet and outlet faces ($P_{fluid} = P_{inlet} - P_{outlet}$)

The results are as follows:

The study mentioned as reference is the work of Jarret and Kim.

Table 3.2. Comparison of the results from the validation study

	Reference study	**Validation study**
P_{fluid} (Pa)	2948	3037
T_{avg} (K)	306.09	306.12
T_{σ} (K)	2.64	2.507

General Description of the Problem and Physical Model

While designing the cooling plate analyzed in the study, the dimensions of the battery used in the GOUPIL G6 vehicle were taken as a basis. The battery measures 450 (mm) x 810 (mm). Therefore, the cooling plate was created as the same size of the battery pack by using CREO 8.

The determined channel dimensions and mass flow rate values were written in the Taguchi matrix and analysis setups were created. Energy equations, conservation of mass, conservation of momentum, and the equations of the selected turbulence model are numerically solved with the help of ANSYS 2021 R2 Fluent software.

In the study, geometries with three different number of channels (4, 5 and 6 channels) were created. These aforementioned models can be seen in Figure 3.7, 3.8 and 3.9. L_p, W_p, H_p indicated in the figure represent the length, depth, and height of the cooling plate, respectively.

Extensions have been added to the channel inlet and outlet region to improve the fluid flow. L_e denotes the length of the extension at the inlet and outlet.

In order to accurately compare the effect of cooling, the channels are located only within a certain area, regardless of their number. Therefore, the distance between the start of the first channel and the end of the last channel is always set to be 320 (mm) and this is indicated by L_c. In addition, the distance of this specified cooling area from the outer

surfaces of the plate was determined as 15 (mm). Cold plate thickness was kept constant at 20 (mm).

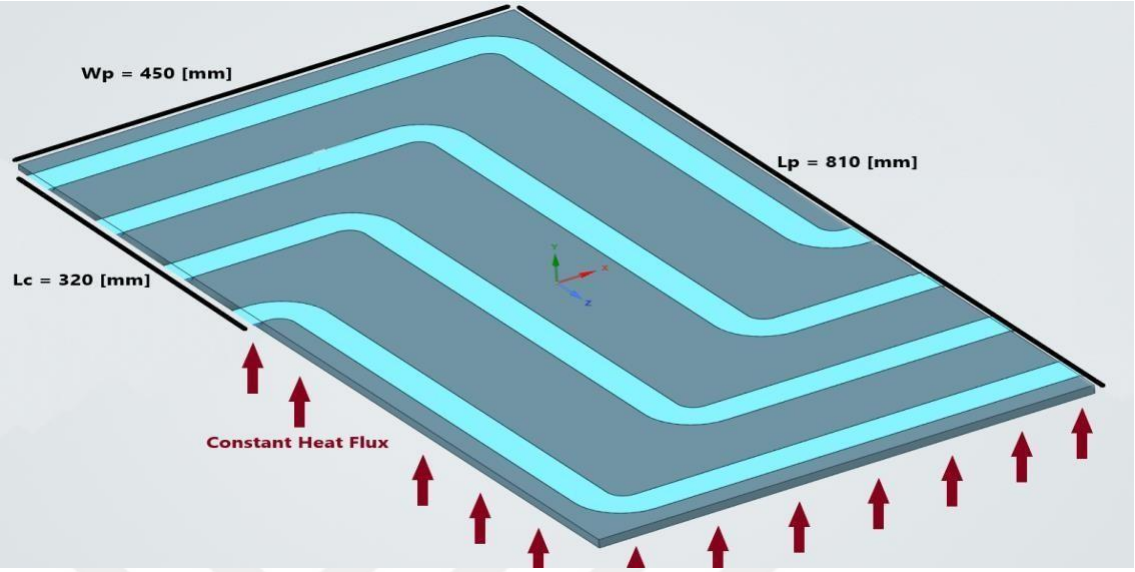


Figure 3.7. 3D geometry of 4-channel cooling plate

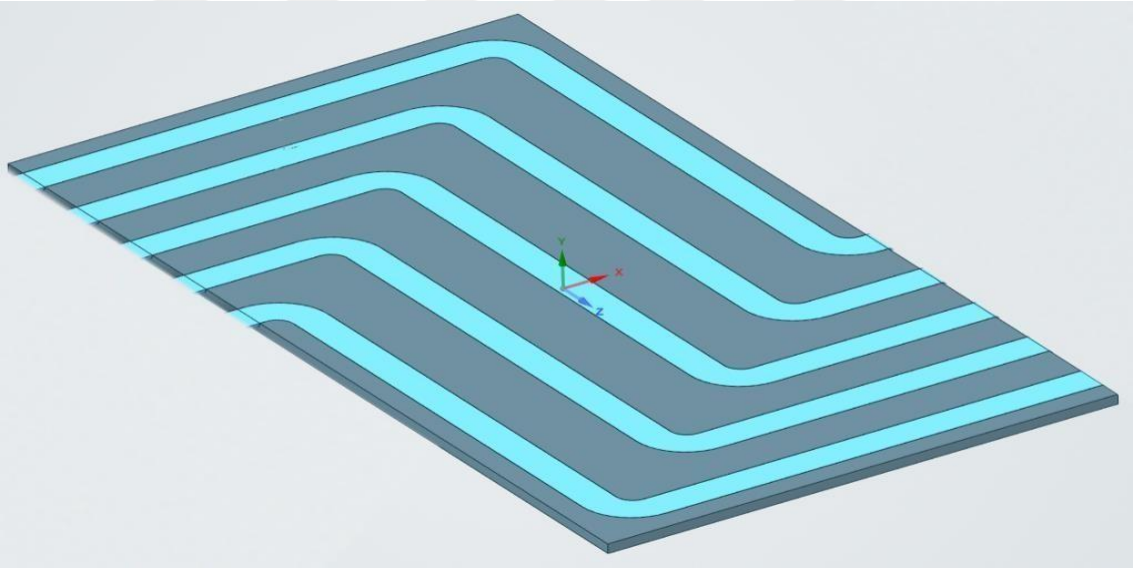


Figure 3.8. 3D geometry of 5-channel cooling plate

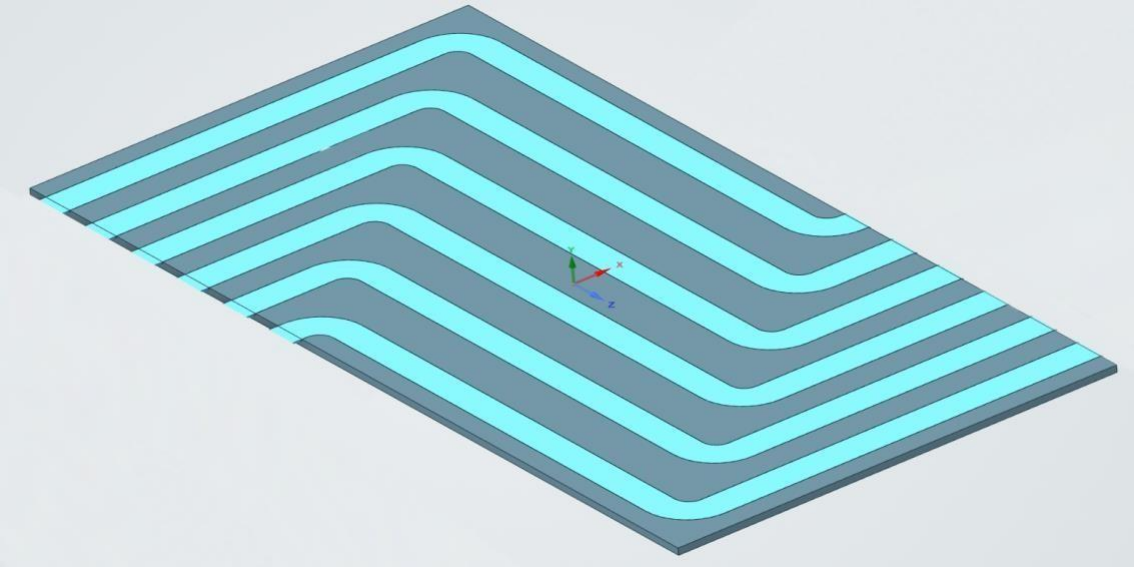


Figure 3.9. 3D geometry of 6-channel cooling plate

The width of the channels has always been kept at the same value, which is 30 (mm), only the height has been increased. The heights used are 10 (mm), 12 (mm) and 14 (mm), respectively. 4, 5 and 6 channels are used in the analyzed geometries.

The analysis were carried out with three different refrigerants, namely water solution with 25% and 50% glycol ratio and water. The type and thermal properties of plate, cooling channel and refrigerant are as given in between Table 3.3 – Table 3.4.

Table 3.3. Thermal properties of Al

Plate and cooling channel material:	Al
Density (kg/m^3) :	2719
Specific heat (J/(kg) K) :	871
Thermal conductivity (W/(m K)) :	202.4

Table 3.4. Thermal properties of cooling fluids

	Water	**EGW 25**	**EGW 50**
Density (kg/m3) :	998.2	1028	1061
Specific heat (J/(kg) K) :	4182	3827	3348
Thermal conductivity (W/(m K)) :	0.6	0.493	0.3935
Viscosity (kg/(m s)) :	0.001003	0.001564	0.002974
Freezing temperature (°C):	0	-10	-36

Taguchi matrices were used for the optimization in the study. As in the Taguchi method, the properties that change are called parameters and the different values they take are called levels (Freddi & Salmon 2019). Thus, since there are three parameters, A, B, and C, and each parameter has three levels, the matrix has three different levels. Since laminar and turbulent flows were examined in the analysis, a separate matrix was applied for each situation. Therefore, the C parameter of the mass flow rate is shown in Table 3.5 for two different levels.

Table 3.5. Values used in the study

Parameters	**Levels**		
(A)Number of channels:	4	5	6
(B)Height of the channels (mm):	10	12	14
(C)Mass flow rate (Laminar) (kg/s):	0.032	0.08	0.16
(C)Mass flow rate (Turbulent) (kg/s):	0.8	1	1.2

3.2.1 Assumptions

Since the geometry is symmetrical, only half of it is modeled and a symmetry boundary condition is defined for the upper part of the cooling plate. A constant heat flow of 3020 (W/m^2) is applied to the lower part of the plate. However, since the heat produced by the battery is not constant, a generic thermal model of the battery was created using the Amesim software and optimized by comparing it with the real-time experiment.

Following this, the constant current value was given into the model and the constant heat flow value used in the analysis was determined. Adiabatic boundary condition is applied to the side walls of the solid domain (cold plate).

Since the surfaces between the cooling plate and the channels are the surfaces that are used in common, interface definitions were made on these surfaces and mesh interfaces were created in fluent in order for the software to solve the heat transfer in these areas. In order to regulate the flow more quickly, the channels at the inlets and outlets have been extended by 300 (mm), ten times the channel width. While the definition of symmetry was made on the upper part of these elongated channels, the adiabatic boundary condition was applied on the lower parts.

Computational Fluid Dynamics (CFD)

CFD is a numerical solution method used in the analysis of complex problems involving fluid-fluid, fluid-solid and fluid-gas interactions and showing how the fluid will behave in the specified problems (Simscale 2022).

The equations used in the analysis are the Navier – Stokes equations developed in the 1800s. Equations describe how velocity, pressure, temperature, and density are related in fluid. These equations expressing a set of combined differential equations and can be solved in theory using various mathematical methods for a given flow problem but in practice it is almost impossible to solve these equations analytically. In the past, engineers made approximations and assumptions and turned these equations into a set of equations that they could solve. Recently, equations have been solved using various techniques such as finite difference, finite volume, finite element, and spectral methods. This field is called Computational Fluid Dynamics or CFD (Hall 2021, Li & Nielsen 2011).

CFD is preferred for many reasons, used in design and validation studies, thermal and combustion analyzes in the aerospace, defense, aerospace, automotive and energy sectors when the possibility of experimentation is limited or not available. These are:

- Giving fast and reliable results compared to experiments

- Cheaper than other methods
- Allowing more detailed examinations in the flow region
- Safer to conduct examinations in studies in the fields of combustion and nuclear
- Shorter development stages
- Significantly reduce the amount of prototypes

Before performing the analysis, certain stages of CFD should be known and the working pathway should be shaped according to these steps which can be seen in Figure 3.10.

In the first step, the purpose of the project is determined, and suggestions are made about how to solve the problem in this direction. After that, the geometry to be solved is created using a CAD software. At this step, simplifications should be made that will not affect the result but will shorten the analysis time. The flow field is discretized into grid. Thereis no optimum mesh structure and number of elements for all cases. These vary accordingto the definition of the problem and shape of the geometry. It should be noted that the probability of getting wrong results with an incorrectly formed network structure is veryhigh. After the solution mesh is created, the analysis is performed by giving the boundaryand initial conditions. Finally, with the help of postprocessing, the results are obtained and interpreted (Slater 2021).

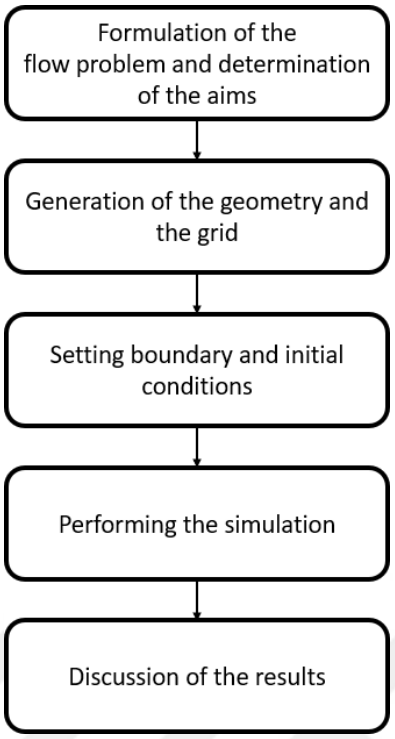


Figure 3.10. Steps of CFD analysis (Slater 2021)

Numerical Model

Mesh Independence Study

The results obtained from the analysis vary up to a certain number of elements. This value, where the change is so small that it is negligible and almost unobservable, is called number of mesh-independent elements (Gardiner 2017). Increasing the number of elements after this limit does not make the solution more accurate but also causes the solution time to prolong and the analysis to be more costly. For this reason, it is important to determine the number of elements before the studies to be carried out.

For this study, four different mesh structures were created and analyzed for turbulent flow with a mass flow rate of 1 (kg/s), for geometry with four channels and a height of 10 (mm). At the end of the analysis, the pressure difference between the inlet and the outlet and maximum temperature on heat flux surface were obtained and visualized.

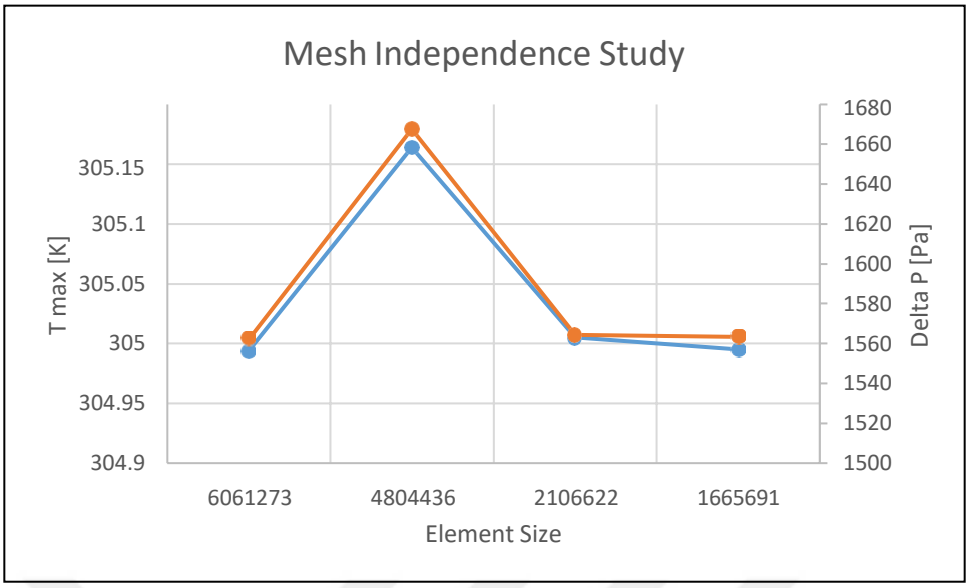


Figure 3.11. Mesh independence study

As a result of the studies, since there was not much change after the mesh structure with the number of 2 200 000 elements according to the ones shown in Figure 3.11, this number of elements was determined as the most appropriate and main analyzes were made according to this mesh structure.

Tetrahedral elements are used in the mesh structure seen in Figure 3.12 and Figure 3.13. Inflation layers have been added in order to condense the mesh structure on the channel surfaces and to provide better resolution of the flow.

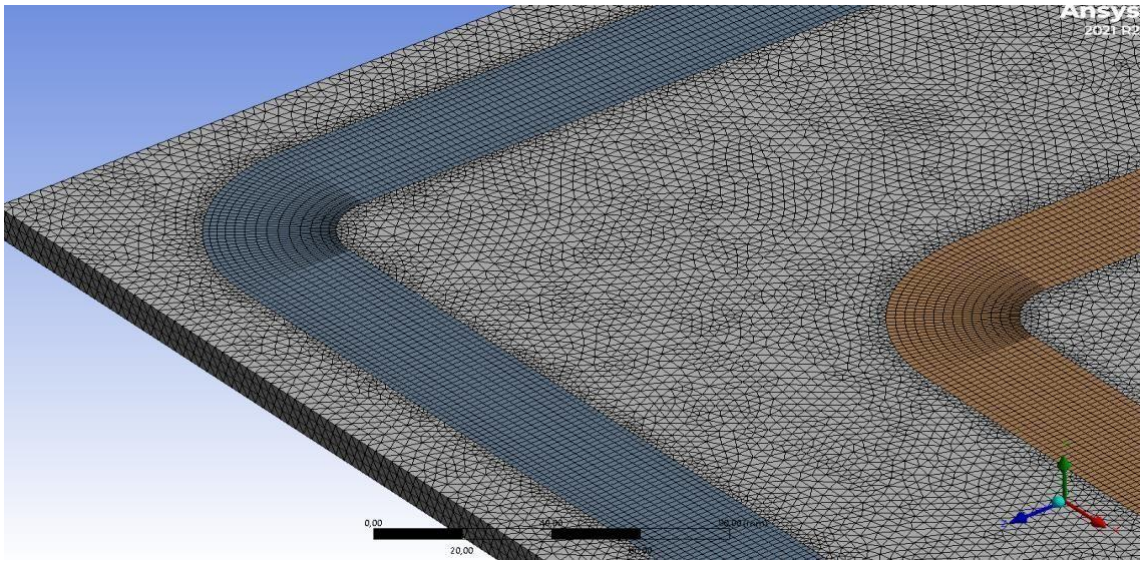


Figure 3.12. Obtained mesh structure

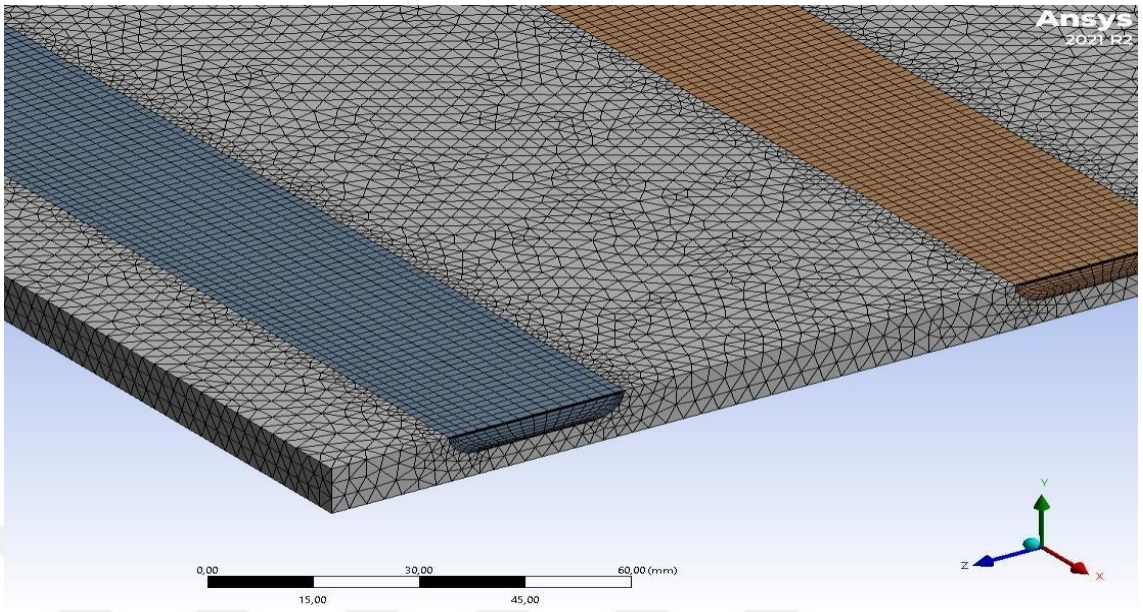


Figure 3.13. Obtained mesh structure in detail

Boundary Conditions and Conservation Equations

In this study, both laminar and turbulent flow were investigated. In order to obtain simpler solutions, assumptions were made that;

- The flow is incompressible, three-dimensional and in a continuous regime
- The properties of the solid and the fluid don't change with temperature.

The conservation equations used in numerical analysis are given below (Umur 2009, White 2006).

Continuity:

$$\frac{\partial u}{\partial x}+\frac{\partial v}{\partial y}+\frac{\partial w}{\partial z}=0 \tag{3.1}$$

x – momentum:

$$\rho\left(u\frac{\partial u}{\partial x}+v\frac{\partial u}{\partial y}+w\frac{\partial u}{\partial z}\right)=-\frac{\partial P}{\partial x}+\rho g_x+\mu\left(\frac{\partial^2 u}{\partial x^2}+\frac{\partial^2 u}{\partial y^2}+\frac{\partial^2 u}{\partial z^2}\right) \tag{3.2}$$

y – momentum:

$$\rho\left(u\frac{\partial v}{\partial x}+v\frac{\partial v}{\partial y}+w\frac{\partial v}{\partial z}\right)=-\frac{\partial P}{\partial y}+\rho g_y+\mu\left(\frac{\partial^2 v}{\partial x^2}+\frac{\partial^2 v}{\partial y^2}+\frac{\partial^2 v}{\partial z^2}\right) \quad (3.3)$$

z – momentum:

$$\rho\left(u\frac{\partial w}{\partial x}+v\frac{\partial w}{\partial y}+w\frac{\partial w}{\partial z}\right)=-\frac{\partial P}{\partial z}+\rho g_z+\mu\left(\frac{\partial^2 w}{\partial x^2}+\frac{\partial^2 w}{\partial y^2}+\frac{\partial^2 w}{\partial z^2}\right) \quad (3.4)$$

Energy:

$$\rho c_p\left(u\frac{\partial T}{\partial x}+v\frac{\partial T}{\partial y}+w\frac{\partial T}{\partial z}\right)=k\left(\frac{\partial^2 T}{\partial x^2}+\frac{\partial^2 T}{\partial y^2}+\frac{\partial^2 T}{\partial z^2}\right) \quad (3.5)$$

where ρ is the density of the fluid (kg/m3), *u, v, w* are the velocity vectors in the x, y, z direction respectively (m/s), c_p the specific heat of the fluid (J/kg K), g the gravitational acceleration (m/s²) where T is the temperature (K) and μ is the dynamic viscosity of the fluid (Ns/m²).

Turbulence Model

Turbulence is a type of fluid flow which refers to irregular motion of the fluid resulting from eddies and vertical currents. Most problems faced by engineers are situations involving turbulent flow. It usually occurs in fluids with low viscosity. This is because after a certain time, the kinetic energy of the fluid overcomes the damping effect of its viscosity. In this type of flow, due to the formation of unstable eddies in many dimensions, friction, and the resulting drag increases. This increases the energy requiredfor the pump.

The Reynolds number is one of the dimensionless numbers that determines whether a flow is turbulent or not and it can be defined as the ratio of inertial forces to viscous forces. Reynolds number can be defined as (Kılıç and Yiğit 2018):

$$Re=\frac{u_m * D_h}{\nu} \quad (3.6)$$

where u_m is average flow velocity (m/s), D_h is the hydraulic diameter (m) and ν is the kinematic viscosity (m²/s).

Table 3.6. Flow type conditions depending on Reynolds number (Kılıç and Yiğit 2018)

	Flow Type	**Reynolds Number**
Internal	Laminar	$Re \leq 2300$
	Transition	$2300 < Re \leq 4000$
	Turbulent	$Re > 4000$
External	Turbulent	$Re > 5 * 10^5$

The eddies and rotations that occur in the flow due to turbulence increase the heat transfer as they disturb the growth of boundary layer on heat exchange surfaces. Therefore, they are preferred in heat exchanger designs. However, since these eddies create sudden pressure drops, the systems need to be carefully studied. Various turbulence models have been developed to solve these complex structures, which are difficult to solve analytically. These models are gathered under three main headings. These are:

1. Reynolds-Averaged Navier-Stokes (RANS)
2. Large Eddy Simulation Turbulence Model (LES)
3. Direct Numerical Simulation (DNS)

DNS resolves all scale of motion up to the Kolmogorov scale. LES can solve most of the scales and very small eddies are modeled. RANS can only resolve large-scale eddies. For this reason, the complexity and cost of analysis increases as one moves from RANS to LES and DNS (Tu et al. 2023).

Considering the complexity and possible cost of the study, it was decided to use RANS in the study and detailed information about this model was given.

Reynolds-Averaged Navier-Stokes (RANS)

It has been observed that eddies in turbulent flow cause significant fluctuations around the mean values of instantaneous values of velocity, temperature, pressure and even density in compressible flows. For this reason, in order to find the desired speed, temperature and pressure values, the average values according to time and the swash values should be added as shown in the indices between 3.6 – 3.9. Here, u_i shows the

values at a certain moment, $\bar{u}_i$ indicates the average values according to the time and u' describes the fluctuation values (Umur 2009).

$$u_i = \bar{u} + u' \tag{3.7}$$

$$v_i = \bar{v} + v' \tag{3.8}$$

$$T_i = \bar{T} + T' \tag{3.9}$$

$$P_i = \bar{P} + P' \tag{3.10}$$

and the average value according to time can be express as:

$$\bar{u} = \frac{1}{t_0}\int_0^t u\,dt \tag{3.11}$$

where t_0 indicates the average time period. Accordingly, the time-averaged Navier - Stokes equation is:

$$\rho\left(\frac{\delta \bar{u}}{\delta t} + \bar{u}_k \frac{\delta \bar{u}}{\delta x_k}\right) = -\frac{\delta \bar{p}}{\delta x_i} + \frac{\delta}{\delta x_j}\left(\mu \frac{\delta \bar{u}}{\delta x_j}\right) + \frac{\delta R_{ij}}{\delta x_j} \tag{3.12}$$

where R_{ij} equals to $(-\rho\overline{u_i' u_j'})$ and express the Reynolds stresses.

The equations expressing the 3-dimensional turbulent flow in the steady regime in cartesian coordinates are as follows (Umur 2009).

Continuity:

$$\frac{\partial(\bar{\rho}\bar{u})}{\partial x} + \frac{\partial(\bar{\rho}\bar{v})}{\partial y} + \frac{\partial(\bar{\rho}\bar{w})}{\partial z} = 0 \tag{3.13}$$

x – momentum:

$$\frac{\partial(\bar{\rho}\bar{u})}{\partial x} + v\frac{\partial(\bar{\rho}\bar{u})}{\partial y} + w\frac{\partial(\bar{\rho}\bar{u})}{\partial z}\Big) = -\frac{\partial \bar{P}}{\partial x} + \rho g_x + \frac{\partial}{\partial x}\left((\mu + \mu_t)\frac{\partial u}{\partial x}\right) + \frac{\partial}{\partial y}\left((\mu + \mu_t)\frac{\partial u}{\partial y}\right) + \frac{\partial}{\partial z}\left((\mu + \mu_t)\frac{\partial u}{\partial z}\right) \tag{3.14}$$

y – momentum:

$$\frac{\partial(\bar{\rho}\bar{u}\bar{v})}{\partial x} + v\frac{\partial(\bar{\rho}\bar{v}\bar{v})}{\partial y} + w\frac{\partial(\bar{\rho}\bar{v}\bar{w})}{\partial z}) = -\frac{\partial \bar{P}}{\partial y} + \rho g_y + \frac{\partial}{\partial x}((\mu + \mu_t)\frac{\partial \bar{v}}{\partial x}) + \frac{\partial}{\partial y}((\mu + \mu_t)\frac{\partial \bar{v}}{\partial y}) + \frac{\partial}{\partial z}((\mu + \mu_t)\frac{\partial \bar{v}}{\partial z}) \quad (3.15)$$

z – momentum:

$$(\frac{\partial(\bar{\rho}\bar{u}\bar{w})}{\partial x} + v\frac{\partial(\bar{\rho}\bar{v}\bar{w})}{\partial y} + w\frac{\partial(\bar{\rho}\bar{w}\bar{w})}{\partial z}) = -\frac{\partial \bar{P}}{\partial z} + \rho g_z + \frac{\partial}{\partial x}((\mu + \mu_t)\frac{\partial \bar{w}}{\partial x}) + \frac{\partial}{\partial y}((\mu + \mu_t)\frac{\partial \bar{w}}{\partial y}) + \frac{\partial}{\partial z}((\mu + \mu_t)\frac{\partial \bar{w}}{\partial z}) \quad (3.16)$$

Energy:

$$\frac{\partial}{\partial x}(\bar{\rho}\bar{u}C_p\bar{T}) + \frac{\partial}{\partial y}(\bar{\rho}\bar{v}C_p\bar{T}) + \frac{\partial}{\partial y}(\bar{\rho}\bar{w}C_p\bar{T}) = \frac{\partial}{\partial x}((k_i + k_t)\frac{\partial \bar{T}}{\partial x}) + \frac{\partial}{\partial y}((k_i + k_t)\frac{\partial \bar{T}}{\partial y}) + \frac{\partial}{\partial z}((k_i + k_t)\frac{\partial \bar{T}}{\partial z}) + Q_V \quad (3.17)$$

where μ_t is the eddy viscosity and k_t is the turbulent conductivity (Umur 2009).

Design of Experiment

Experimental studies are necessary for a study to be scientific, but these studies require a long time. In order for the studies to be accurate, to reduce the cost and to save time, various experimental designs should be used. These experimental designs are generally examined under two main headings (Gökçe and TaĢgetiren 2009).

These are:

- Classical or passive methodology
- Statistical or active methodology

Design of Experiment with Classical Methodology

The methodology, which is carried out by changing a single parameter in each experiment and keeping the other independent parameters constant, and thus examining the effect of the changing parameters on the system, is called the classical methodology (Gökçe and TaĢgetiren 2009). The schematic explanation of the method is as seen in the Figure 3.14.

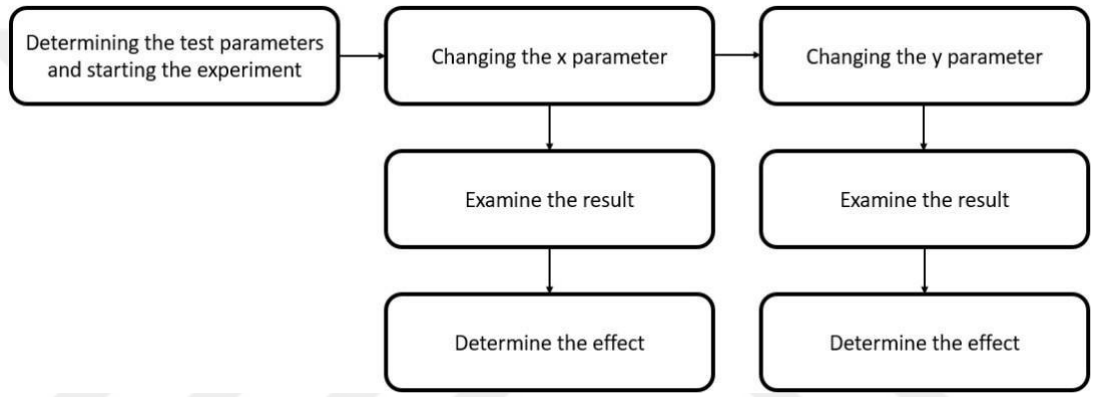


Figure 3.14. Stages of the classical methodology (Gökçe and TaĢgetiren 2009)

However, in this methodology type, noncontrollable (external factors) are not taken into account while designing the experiment. Another important point is that since each changed parameter corresponds to an experiment, time and cost may increase depending on the experimental design.

Design of Experiment with Statistical Methodology

The inadequacy of passive experiment design methods has been eliminated by statistical experiment design methods. This experimental design method is divided into three titles (Gökçe and TaĢgetiren 2009).

These are:

- Full factorial
- Fractional factorial
- Taguchi method

Full Factorial

It represents the combinations of experiments with at least two parameters and each of these parameters having at least two levels. For example, with four parameters, each of which has three levels, combinations of the experiment can be calculated as 3x3x3x3=81. This design is based on the principle of experiment repetition, random selection of the experiment order, and experiment blocking. The aim is to prevent unknown and uncontrollable errors from affecting the experiment.

Fractional Factorial

In this type of experiment design, combinations of all levels are tried one by one. But the realization of this design takes a lot of time. Therefore, it is very costly compared to others. In order to shorten the experiment time, the total number of experiments can be reduced proportionally to $(1/2)$, $(1/4)$ or $(1/8)$ but this method is left to the preference of the researcher.

Taguchi

In the Taguchi method, the design and optimization of the experiment to be used is determined by the design of the parameters, design of the system and design of the tolerance. It is the most commonly used method as it is very convenient for determining the optimum design combination between different levels of different parameters.

In the first step of the method, the information available in system design is compiled and various technologies are researched to see if they can be used in the experiment. The aim is to provide the highest satisfaction with the least cost.

The second step, parameter design, is based on the improvement of the process. Parameters are selected at the best levels and noncontrollable effects are determined. The effects of these parameters are minimized. Blocking of parameters is performed in this step. For this, orthogonal arrays developed by Taguchi are used. According to those given

in Table 3.7, a researcher has seven parameters and two levels for each parameter, the person should select the L8 sequence.

Table 3.7. Taguchi's orthogonal array table (Gökçe and TaĢgetiren 2009)

Number of Parameters	Number of Levels							
	2		3		4		5	
	Prm=2, S=2 Prm=3, S=2	L4	Prm=2, S=3 Prm=3, S=3 Prm=4, S=3	L9	Prm=2, S=4 Prm=3, S=4 Prm=4, S=4 Prm=5, S=4	L16	Prm=2, S=5 Prm=3, S=5 Prm=4, S=5 Prm=5, S=5 Prm=6, S=5	L25
	Prm=4, S=2 Prm=5, S=2 Prm=6, S=2 Prm=7, S=2	L8	Prm=5, S=3 Prm=6, S=3 Prm=7, S=3 Prm=8, S=3	L18	Prm=6, S=4 Prm=7, S=4 Prm=8, S=4 Prm=9, S=4 Prm=10, S=4	L32	Prm=7, S=5 Prm=8, S=5 Prm=9, S=5 Prm=10, S=5 Prm=11, S=5 Prm=12, S=5	L50
	Prm=8, S=2 Prm=9, S=2 Prm=10, S=2 Prm=11, S=2	L11	Prm=9, S=3 Prm=10, S=3 Prm=11, S=3 Prm=12, S=3 Prm=13, S=3	L27				
	Prm=12, S=2 Prm=13, S=2 Prm=14, S=2 Prm=15, S=2	L16	Prm=14, S=3 Prm=15, S=3 Prm=16, S=3 Prm=17, S=3 Prm=18, S=3 Prm=19, S=3 Prm=20, S=3 Prm=21, S=3 Prm=22, S=3 Prm=23, S=3	L36				
	Prm=16, S=2 Prm=17, S=2 Prm=18, S=2 Prm=19, S=2 Prm=20, S=2 Prm=21, S=2 Prm=22, S=2 Prm=23, S=2 Prm=24, S=2 Prm=25, S=2 Prm=26, S=2 Prm=27, S=2 Prm=28, S=2 Prm=29, S=2 Prm=30, S=2 Prm=31, S=2	L32						

In the tolerance design, which is the last step, additional studies are carried out if the desired goal is not achieved in the parameter determination studies.

In Taguchi the loss function, also called the noise ratio, exists in the form of three different functions to statistically evaluate the results obtained. These are,

Smaller is better:

$$S/N = -10 \log \left[\frac{1}{n} \sum_{i=1}^{n} y^2 \right] \quad (3.18)$$

Bigger is better:

$$S/_N = -10\log\left[\frac{1}{n}\sum_{i=1}^{n}\frac{1}{y_i^2}\right] \quad (3.19)$$

Nominal is better:

$$S/_N = 10\log\left[\frac{1}{n}\sum_{i=1}^{n}\frac{\bar{y}^2}{S^2}\right] \quad (3.20)$$

$$\bar{y} = \frac{1}{n}\sum_{i=1}^{n} y_i \quad (3.21)$$

$$S^2 = \frac{1}{n-1}\sum_{i=1}^{n}[y_i - \bar{y}]^2 \quad (3.22)$$

where y_i represents the i[th] observation value of the performance characteristic, n represents the number of tests in each trial, $\bar{y}$ represents the mean of the observation values, and S^2 represents the variance of the observation values, and the variance of the result decreases as the S/N ratio increases. Whichever method is adopted as the evaluation type, the largest S/N ratio indicates the design with the best experimental result.

The steps to be followed in order to use the Taguchi method are as follows (Gökçe and TaĢgetiren 2009):

- Identification of the problem
- Selection of the noise ratio and determination of the measurement system
- Determination of test parameters and their levels
- Separation of parameters into controllable and noncontrollable
- Controlling whether there is interaction between parameters
- Choosing the appropriate orthogonal array for the experiment
- Selection of quality loss functions and performance statistics
- Performing the experiments in certain repetitions and recording the results
- Determination of the best parameter level combination according to the desired result, conducting the validation test and conclusion

Column effect method is used to examine the effective parameters as a result of the experiments.

In the optimization problem, if the goal is to optimize a single performance response, the traditional Taguchi method can be used. However, when faced with a multi-response optimization problem, hybrid approaches in which multi-criteria decision making methods are used together with Taguchi should be adopted. Thus, optimization can be performed with a meaningful approach by converting more than one parameter into a single answer. One of these hybrid approaches is Taguchi - Grey Relation Analysis. Here, the gray relationship is related to the similarities and differences between any two elements in a particular system, and if the changes between these two elements are significant and meaningful, there is a high correlation, while on the contrary, there is a lower relationship (Wang 2019; Ozdemir Kucuk 2023).

The S/N ratios of each response obtained in the GRA hybrid method are calculated and the deltas of each parameter are summed. Existing data is normalized between 0 and 1. The gray correlation coefficient is calculated from the normalized matrix representing the correlation between the desired and actual experimental data, and the gray correlation analysis is performed by calculating the weight coefficients of each parameter according to the total delta value (Ozdemir Kucuk 2023).
In this study, since high cooling performance and low pressure drop are desired, the objective function "smaller is better", which is one of three different criteria that maximizes the values of the system, was adopted. Equation (3.23) was used to normalize the output parameters (Chamoli et al. 2016).

$$y_i(k) = \frac{\max_i x_i^0(k) - x_i^0(k)}{\max_i x^0(k) - \min_i x^0(k)} \tag{3.23}$$

where, $y_i(k)$ represents the normalization value of the grey relational analysis, $\max_i x^0(k)$ and $\min_i x^0(k)$ are the largest and smallest values of $x_i(k)$ for the kth response, respectively. In addition, the symbols i and k represent the number of experiments and the number of responses, respectively (Asafa et al. 2013).

After the normalization of the data, the gray correlation coefficient (ξ_i), is calculated with the help of Equation (3.24).

$$\xi_i(k) = \frac{\Delta_{min} + \phi\,\Delta_{max}}{\Delta_{0i}(k) + \phi\,\Delta_{max}} \tag{3.23}$$

$$\Delta_{0i}(k) = \|y_0(k) - y_i(k)\| \tag{3.24}$$

$$\Delta_{max} = max_{\forall j \varepsilon i}\, max_{\forall k}\, \|y_0(k) - y_i(k)\| \tag{3.25}$$

$$\Delta_{min} = min_{\forall j \varepsilon i}\, min_{\forall k}\, \|y_0(k) - y_i(k)\| \tag{3.26}$$

$\Delta_{0i}(k)$ describes the deviation between $y_0(k)$ and $y_i(k)$ and Eq (3.25) and (3.26) can be used to calculate Δ_{max} and Δ_{min}, respectively. ϕ, which is defined as the discriminant coefficient, is a value in the range between 0 to 1 and ϕ was taken as 0.5 (Bademlioglu 2020). Grey Relational Degree (γi) with normalized weight factor is calculated by Equation (3.27).

$$\gamma_i = \frac{1}{n}\sum_{k=1}^{n} w_k \xi_i(k) \tag{3.27}$$

where n represents the number of process responses. A high γ_i designates a strong correlation between $y_0(k)$ and $y_i(k)$. γ_i is used to determine the closeness of the compared serial value to the reference serial value. If the two series have the same values,

$\gamma_i = 1$.

In Eq (3.27), $\sum^{n}{}_{k=1} w_k = 1$, is the normalized weighting factor for each response. In order to reduce the multi-response optimization problem to a single response, the effect ratio of each output parameter's weight factor should be considered. It can be calculated by Eq (3.28)

$$w_i = \frac{\sum_{j=1}^{p} Delta_{i,j}}{\sum_{i=1}^{t}\sum_{j=1}^{p} Del_{i,j}a} \tag{3.28}$$

where, t represents the number of responses, p describes the number of parameters, and Delta is the range of S/N.

The GRG value to be used in the last phase of the optimization can be calculated using equation 27.

$$GRG(EGW25) = 2.337229 * GRC\ T_{max} + 27.12855 * GRC\ T_{ss} * 70.53422 * GRC\ \Delta P \quad (3.29)$$

Creation of the Taguchi Statistical Design

In this study, numerical CFD analysis were used to determine the most suitable design parameters for the cooling plate of the existing lithium-ion battery for laminar and turbulent flow conditions. For both conditions, three parameters were selected as number of channels, channel height and fluid flow rate. The levels of these parameters are given in the Table 3.9 – 3.10.

Table 3.8. Level combinations in the Taguchi L9 statistical design

Factors / Levels	**A**	**B**	**C**
1	1	1	1
2	1	2	2
3	1	3	3
4	2	1	2
5	2	2	3
6	2	3	1
7	3	1	3
8	3	2	1
9	3	3	2

After that, the parameters and levels are written in the relevant places in this matrix, and the matrix sequence to be used in CFD analysis is shown in the table.

Table 3.9. Orthogonal array for laminar study

Factors / Levels	K	L	M
1	4 channels	10 mm	0.032
2	4 channels	12 mm	0.08
3	4 channels	14 mm	0.16
4	5 channels	10 mm	0.08
5	5 channels	12 mm	0.16
6	5 channels	14 mm	0.032
7	6 channels	10 mm	0.16
8	6 channels	12 mm	0.032
9	6 channels	14 mm	0.08

Table 3.10. Orthogonal array for turbulent study

Factors / Levels	A	B	C
1	4 channels	10 mm	0.8
2	4 channels	12 mm	1
3	4 channels	14 mm	1.2
4	5 channels	10 mm	1
5	5 channels	12 mm	1.2
6	5 channels	14 mm	0.8
7	6 channels	10 mm	1.2
8	6 channels	12 mm	0.8
9	6 channels	14 mm	1

While determining the flow values, the Reynolds number was calculated for each condition, and it was verified that it was less than 2300 for laminar conditions. The formulas used in the calculation are as given below.

$$D_h = \frac{4\,A_c}{P} \tag{3.30}$$

$$\dot{m} = \rho * u * A_c \tag{3.31}$$

$$Re = \frac{u * D_h * \rho}{\mu} \tag{3.32}$$

where, $\dot{m}$ is the flow of water entering a channel (kg/s), A_c is the cross-sectional area of the channel perpendicular to the flow (m²), P is the circumference of the channel perpendicular to the flow, and u is the average velocity of the water (m/s).

Table 3.11. Verified Reynolds numbers for each case and fluid type

	LAMINAR			**TURBULENT**		
	Water	**EGW 25**	**EGW 50**	**Water**	**EGW 25**	**EGW50**
L1	446.74	286.50	150.67	11168.53	7162.43	3766.66
L2	1082.25	694.05	365.00	13528.17	8675.68	4562.46
L3	2099.47	1346.40	708.06	15746.01	10097.98	5310.44
L4	893.48	572.99	301.33	11168.53	7162.43	3766.66
L5	1731.61	1110.49	583.99	12987.05	8328.65	4379.96
L6	335.91	215.42	113.29	8397.87	5385.59	2832.23
L7	1489.14	954.99	502.22	11168.53	7162.43	3766.66
L8	288.42	184.97	97.27	7215.03	4627.03	2433.31
L9	699.65	448.69	235.96	8747.78	5609.99	2950.24

In order to decide which of the results found is the most appropriate, it is more useful to consider the thermal resistance, the required pump power, the maximum temperature, and pressure loss, in comparisons.

$$R_{thermal} = \frac{T_{max} - T_{in}}{q * A} \tag{3.33}$$

where $R_{thermal}$ is the thermal resistance (K/W), T_{max} is the maximum temperature of the heat flux surface (T_{max}) and T_{in} is the inlet temperature of the fluid to the channel (T_{in}), the constant heat flux (W/m^2) represented by q applied to the bottom of the plate and A is the surface area the bottom.

$$W_{pump} = V * \Delta P \tag{3.34}$$

V in the formula represents the volume flow and ΔP represents the pressure difference.

One-dimensional Generic Model of the Battery

Calculating the heat which is produced in the batteries as an average value is not correct in reality. Because this value depends on more than one parameter such as time, ambient temperature, used cycle, percentage of state of charge. These parameters cause different temperature outputs by changing the internal resistance. However, to carried out the analysis, a constant mean value must be found.

Amesim software was used in order to obtain this value more easily and not to resort to long-term experimental tests for every finding needed. In parallel with the multi-physical analysis, charge and discharge tests were carried out and the results were compared, and the model was optimized. The testbench modeled as 1D is as seen below.

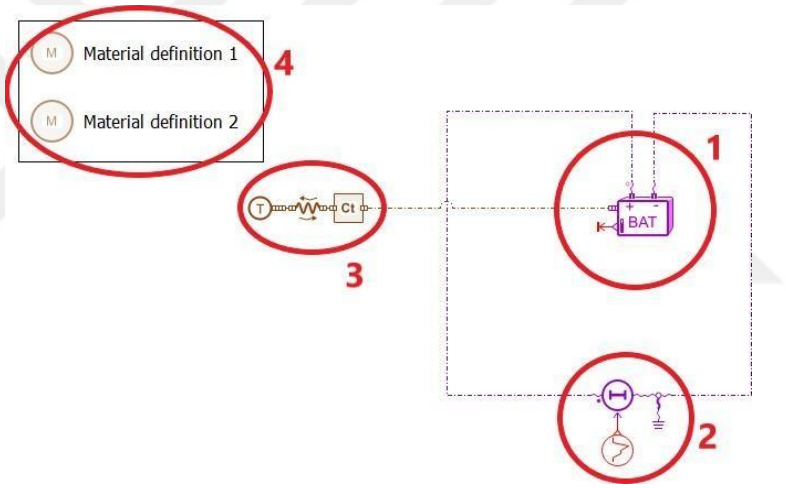


Figure 3.15. Charge/discharge testbench model of G6 battery

The element shown with one is a generic model of the current lithium-ion battery. Considering the ease of design and the data needed, a general modeling was used instead of the cell-based model. The internal resistance and open circuit voltage values obtained from the manufacturer are the values obtained at a single ambient temperature. However, this makes it impossible to perform analyzes at different ambient temperatures. For this reason, the battery model was created based on real data and using the battery pre-sizing tool in Amesim. The mentioned battery pre-sizing tool is as shown in Figure 3.16. The data of the battery to be modeled were entered in the area marked as A and the outputs in

the section indicated with B were calculated and four different graphs based on the temperatures in section C were created by Amesim.

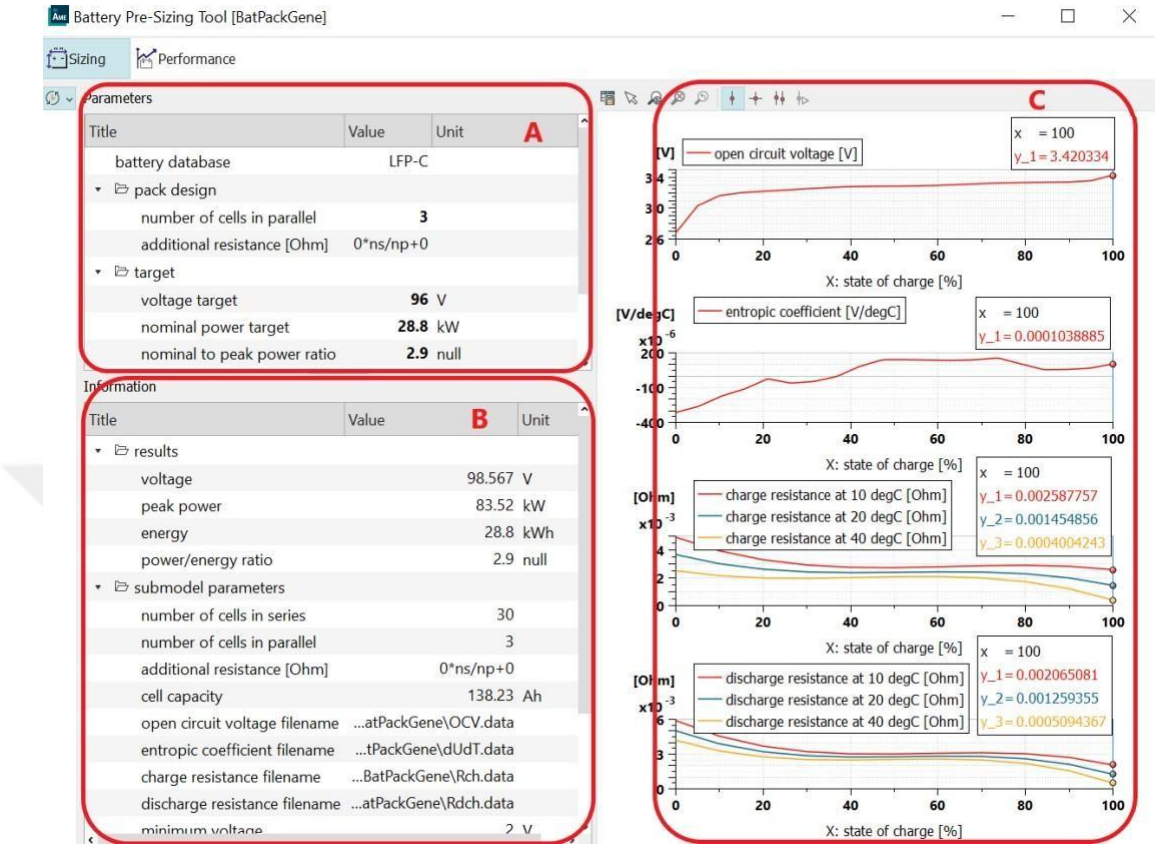


Figure 3.16. Battery pre-sizing tool

Element number two seen in Figure 3.15 is placed for the current input which is 60 [A]. The elements indicated with three are the heat transfer model created to obtain the average temperature outputs required for the comparison of the temperature results. Finally, the fourth elements are used to define the material required to calculate the heat transfer.

Parallel to the AMESIM tests, the charging test was performed in reality by using a testbench. Thermal sensors are connected to the battery and the battery is expected to charge from 0% to 100% SOC. Although the ambient temperature is accepted as 25°C, the mentioned test was carried out in an open environment. For this reason, the outdoor temperature could not be controlled and its effect on the battery could not be fully investigated during the test.

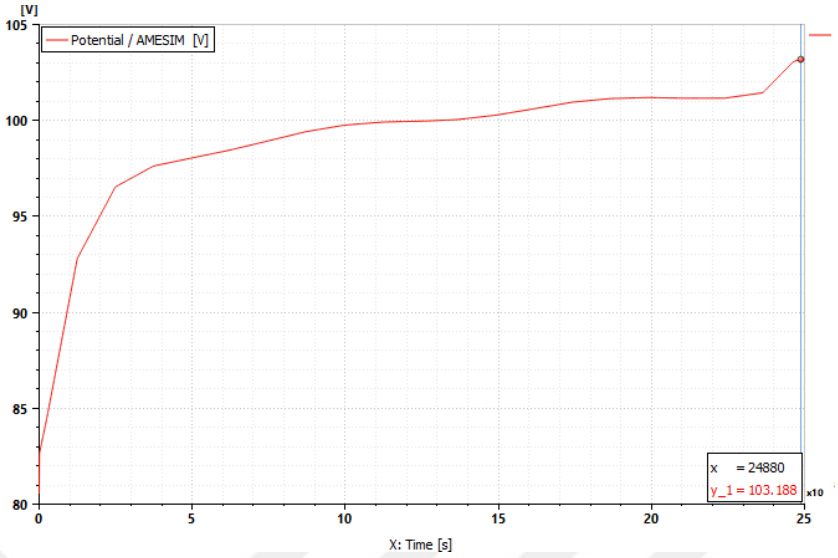


Figure 3.17. Potential graph for AMESIM model

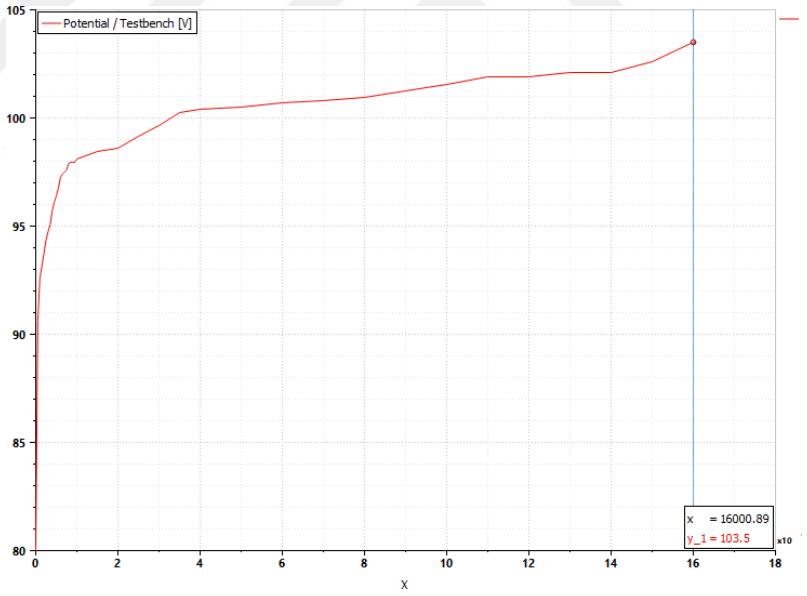


Figure 3.18. Potential graph for testbench

In Figure 3.17 and 3.18, the potential graphics of the current batteries under charging tests performed in Amesim and testbench are given. It was observed that both graphs showed a similar behavior, but since the battery charge times were obtained at different time steps, they could not be gathered under a single graph.

The average temperatures obtained from the two tests are given in the graph below. One of the reasons for the current deviation in the mean temperature outputs is that the battery modeled in AMESIM is constructed using a pre-sizing tool in certain approaches. This tool applies real data to mathematical models and obtains graphs indicated with C in Figure 3.16 for certain temperature ranges. Due to this approach, a certain deviation is expected. Another reason is that, as mentioned before, the environment was not isolated for the testbench. Therefore, it can be assumed that the test is affected by the ambient temperature. Considering these conditions, the validation of the 1D model created was approved and used for further tests.

Table 3.12. Comparison of temperature outputs

	AMESIM	**TESTBENCH**
Average Battery Temperature [°C]	30.3065	33.1875

The value to be used as a limit condition for Ansys was determined by the AMESIM model. 200 [A] is determined as current input and heat flux value for 50% SOC condition is calculated (Bernardi 1984) with post processing section. The outputs obtained from the analysis are as follows (Figure 3.19).

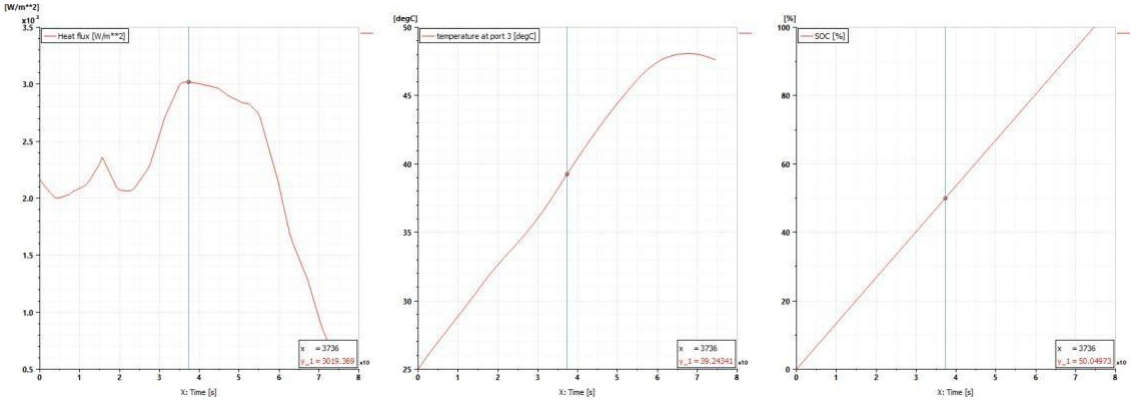


Figure 3.19. Obtained constant heat flux value

4. RESULTS AND DISCUSSION

In this section, the orthogonal experimental designs for laminar and turbulent flow are solved with CFD and the results are compared with the Minitab software using Taguchi method, and the optimum result is reached for both cases. Finally, the temperatures obtained from the optimum designs were compared with the temperature obtained from the battery model, which was validated and modeled with inexperience, without any cooling element.

In the analysis of quality characteristics, there are three different options as "smaller is better", "larger is better" and "nominal is better". In this study, it is desired that the cooling plate of the lithium-ion battery should be low in thermal resistance and the pump power to be used should be selected low, considering the operating cost. For this reason, the choice of “smaller is better” has been made.

The pressure losses obtained from the experiments of each array in the orthogonal array, the maximum temperatures on the surface where the heat flow is defined (representing the battery), the average temperatures and the average speed in the cooling channel are calculated within the Fluent. In the light of these data, necessary pump power and thermal resistance calculations were made. These results for three types of fluids can be examined in table 4.1.

Table 4.1. Result values obtained under laminar flow conditions

	T_{max}			T_{σ}			ΔP		
	Water	**EGW 25%**	**EGW 50%**	**Water**	**EGW 25%**	**EGW 50**	**Water**	**EGW 25%**	**EGW 50**
L1	339.56	346.89	362.00	5.42	6.07	8.14	31.57	44.24	75.68
L2	324.25	329.31	340.26	2.84	3.24	4.81	67.00	87.83	137.63
L3	317.25	320.86	328.11	2.13	2.42	3.07	124.67	160.38	234.76
L4	320.76	326.31	308.89	2.61	3.51	2.37	93.19	125.41	204.83
L5	314.42	317.98	324.62	1.75	2.15	2.95	158.70	205.72	305.58
L6	338.75	345.72	360.11	5.49	6.32	8.49	13.67	19.10	32.50
L7	313.04	316.00	321.91	1.74	2.06	3.05	221.21	288.12	449.05

L8	335.61	342.52	356.22	5.43	6.56	8.91	18.76	25.60	64.64
L9	320.74	325.69	333.58	2.70	3.44	4.67	41.79	55.31	89.28

Table 4.2. Result values obtained under turbulent flow conditions

	T_{max}			T_{σ}			ΔP		
	Water	**EGW 25%**	**EGW 50%**	**Water**	**EGW 25%**	**EGW 50**	**Water**	**EGW 25%**	**EGW 50**
L1	305.44	306.54	309.30	1.02	1.10	1.34	1099.20	1229.84	1444.32
L2	305.23	306.24	308.80	1.03	1.10	1.30	1050.27	1185.10	1396.90
L3	305.13	306.10	308.36	1.03	1.10	1.28	1009.82	1140.10	1361.86
L4	303.58	304.44	306.65	0.54	0.60	0.82	1096.83	1227.72	1441.14
L5	303.51	304.30	306.41	0.54	0.60	0.77	978.00	1104.75	1303.57
L6	304.55	305.93	309.07	0.63	0.75	1.14	355.46	398.72	473.66
L7	303.47	304.07	305.30	0.36	0.42	0.64	1109.72	1244.48	1456.62
L8	304.28	305.14	307.67	0.45	0.59	1.05	371.34	412.44	493.58
L9	304.18	305.00	306.99	0.43	0.54	0.91	384.53	430.71	508.71

When the temperature homogeneity is desired to be examined, the temperature standard deviation of the surface to be examined is calculated and compared. According to the results seen in Tables 4.1 and 4.2, the standard deviation value of the lower surface temperature in turbulent condition is lower than in the laminar condition. This shows that the temperature is more homogeneously distributed in the turbulent condition.

The values differed according to the fluid type. As the ratio of glycol ratio in ethylene glycol solution increased, the maximum temperature formed at the base and the standard deviation of temperature also increased. The reason for this situation can be shown as the decrease in the heat conduction coefficient with the increase in the glycol ratio (Table 3). The lowest temperature was reached with water with the lowest thermal conductivity. When the pressure differences are compared, the lowest basic drops were obtained when the fluid was water, and it was noted that the pressure drop increased as the glycol ratio increased.

The obtained results and calculated values were entered into Minitab and Taguchi was chosen as the experimental design. Optimization analysis was run by choosing the “smaller is better” option. The S/N ratios obtained at the end of the optimization are

presented in Table 4.3. It is aimed to reduce the variability in a process by minimizing the effects of uncontrollable factors (noise factors). Higher values of the signal-to-noise ratio (S/N) indicate that the effects of noise factors are minimized. For this reason, it has been determined that noise factors are minimized and the most significant parameter affecting the system is mass flow rate.

Table 4.3. Signal to noise ratio for laminar flow

T_{max}			T_{σ}			ΔP		
Water	**EGW 25**	**EGW 50**	**Water**	**EGW 25**	**EGW 50**	**Water**	**EGW 25**	**EGW 50**
-50.62	-50.80	-51.17	-14.68	-15.67	-18.21	-29.99	-32.92	-37.58
-50.22	-50.35	-50.64	-9.06	-10.20	-13.65	-36.52	-38.87	-42.77
-50.03	-50.13	-50.32	-6.58	-7.69	-9.73	-41.92	-44.10	-47.41
-50.12	-50.27	-49.80	-8.32	-10.89	-7.48	-39.39	-41.97	-46.23
-49.95	-50.05	-50.23	-4.88	-6.63	-9.38	-44.01	-46.27	-49.70
-50.60	-50.77	-51.13	-14.79	-16.01	-18.58	-22.71	-25.62	-30.24
-49.91	-49.99	-50.15	-4.83	-6.27	-9.68	-46.90	-49.19	-53.05
-50.52	-50.69	-51.03	-14.69	-16.33	-18.99	-25.47	-28.16	-36.21
-50.12	-50.26	-50.46	-8.62	-10.74	-13.39	-32.42	-34.86	-39.01

Table 4.4 Signal to noise ratio for turbulent flow

T_{max}			T_{σ}			ΔP		
Water	**EGW 25**	**EGW 50**	**Water**	**EGW 25**	**EGW 50**	**Water**	**EGW 25**	**EGW 50**
-49.7	-49.73	-49.81	-0.17	-0.83	-2.57	-60.83	-61.8	-63.19
-49.69	-49.72	-49.79	-0.22	-0.83	-2.25	-60.43	-61.48	-62.90
-49.69	-49.72	-49.78	-0.23	-0.83	-2.15	-60.08	-61.14	-62.68
-49.65	-49.67	-49.73	5.37	4.44	1.75	-60.80	-61.78	-63.17
-49.64	-49.67	-49.73	5.33	4.44	2.24	-59.81	-60.87	-62.30
-49.67	-49.71	-49.80	3.95	2.5	-1.15	-51.02	-52.01	-53.51
-49.64	-49.66	-49.69	8.76	7.54	3.93	-60.90	-61.9	-63.27
-49.67	-49.69	-49.76	6.92	4.58	-0.38	-51.4	-52.31	-53.87
-49.67	-49.69	-49.74	7.32	4.73	0.85	-51.7	-52.68	-54.13

In Tables 4.5 and 4.6, S/N ratios, delta values and weight differentials calculatedaccording to the levels of control factors determined in Taguchi analysis are given. Here,the delta value is the difference between the largest and smallest values of the S/N ratioscalculated for each factor. A high delta value of a factor explains that the effect of that

factor on the outcome parameter is also high. The Rank expression given in the tables shows the order of influence of the control factors on the outcome parameters. Weight factors were also calculated for each outcome parameter. The weight factor calculated for the pressure drop has taken a value between approximately 62.58 - 70.53% for each fluid and it was seen to be more dominant than the other result parameters.

Table 4.5. S/N ratios and weight factors according to factor levels of laminar results

T_{max}									
	Water			**EGW 25**			**EGW 50**		
Level	**NOC**	**H_c**	**M**	**NOC**	**H_c**	**M**	**NOC**	**H_c**	**M**
1	-50.29	-50.22	-50.58	-50.43	-50.35	-50.76	-50.71	-50.37	-51.11
2	-50.22	-50.23	-50.15	-50.37	-50.36	-50.29	-50.38	-50.63	-50.3
3	-50.18	-50.25	-49.96	-50.31	-50.38	-50.06	-50.55	-50.64	-50.23
Delta	0.1	0.03	0.61	0.11	0.029	0.7	0.33	0.26	0.88
Rank	2	3	1	2	3	1	2	3	1
Σdelta	0.74			0.84			1.47		
w (%)	1.980251			2.337229			3.898791		
T_σ									
	Water			**EGW 25**			**EGW 50**		
Level	**NOC**	**H_c**	**M**	**NOC**	**H_c**	**M**	**NOC**	**H_c**	**M**
1	-10.11	-9.28	-14.72	-11.19	-10.94	-16.00	-13.86	-11.79	-18.56
2	-9.33	-9.54	-8.67	-11.18	-11.05	-10.61	-11.81	-14.01	-11.51
3	-9.38	-9.99	-5.43	-11.11	-11.47	-6.86	-14.02	-13.9	-9.60
Delta	0.78	0.72	9.29	0.074	0.54	9.14	2.21	2.22	8.99
Rank	2	3	1	3	2	1	3	2	1
Σdelta	10.789			9.75			13.424		
w (%)	28.87152			27.12855			35.60365		
ΔP									
	Water			**EGW 25**			**EGW 50**		
Level	**NOC**	**H_c**	**M**	**NOC**	**H_c**	**M**	**NOC**	**H_c**	**M**
1	-36.14	-38.76	-26.06	-38.63	-41.36	-28.9	-42.59	-45.62	-34.68
2	-35.37	-35.33	-36.11	-37.95	-37.77	-38.57	-42.06	-42.9	-42.67
3	-34.93	-32.35	-44.27	-37.4	-34.86	-46.52	-42.76	-38.89	-50.05
Delta	1.21	6.41	18.22	1.23	6.5	17.62	0.7	6.73	15.38
Rank	3	2	1	3	2	1	3	2	1
Σdelta	25.84			25.35			22.81		
w (%)	69.14822			70.53422			60.49756		

According to the results, the degree of influence of the factors varies according to laminar and turbulent flow conditions. In Table 4.5, Delta=8.996 and M (mass flow rate) factor has the maximum effect on the standard deviation of the temperature calculated using 50% ethylene glycol water mixture, however in Table 4.6, it has been observed that with Delta = 3.7868, the NOC (number of channels) factor is the most dominant value on the same result.

Table 4.6. S/N ratios and weight factors according to factor levels of turbulent results

T_{max}									
	Water			**EGW 25**			**EGW 50**		
Level	**NOC**	**H_c**	**M**	**NOC**	**H_c**	**M**	**NOC**	**H_c**	**M**
1	-49.69	-49.66	-49.68	-49.723	-49.686	-49.711	-49.79	-49.74	-49.79
2	-49.65	-49.67	-49.67	-49.683	-49.692	-49.692	-49.75	-49.76	-49.76
3	-49.66	-49.68	-49.66	-49.678	-49.705	-49.681	-49.73	-49.77	-49.73
Delta	0.04	0.01	0.02	0.044	0.019	0.03	0.06	0.03	0.06
Rank	1	3	2	1	3	2	1	3	2
Σdelta	0.07			0.093			0.15		
w (%)	0.248405			0.331338			0.56255		
T_{σ}									
	Water			**EGW 25**			**EGW 50**		
Level	**NOC**	**H_c**	**M**	**NOC**	**H_c**	**M**	**NOC**	**H_c**	**M**
1	-0.2099	4.6528	3.5684	-0.8279	3.7147	2.0846	-2.3217	1.0363	-1.3663
2	4.887	4.0117	4.1582	3.7909	2.7307	2.7802	0.9481	-0.13	0.1178
3	7.6675	3.6801	4.6181	5.6165	2.1341	3.7147	1.465	-0.815	1.3399
Delta	7.8774	0.9727	1.0497	6.4443	1.5806	1.6301	3.7868	1.8513	2.7062
Rank	1	3	2	1	3	2	1	3	2
Σdelta	9.8998			9.655			8.3443		
w (%)	35.13084			34.3986			31.2939		
ΔP									
	Water			**EGW 25**			**EGW 50**		
Level	**NOC**	**H_c**	**M**	**NOC**	**H_c**	**M**	**NOC**	**H_c**	**M**
1	-60.44	-60.84	-54.41	-61.47	-61.83	-55.37	-62.93	-63.21	-56.86
2	-57.21	-57.21	-57.64	-58.22	-58.22	-58.65	-59.66	-59.69	-60.07
3	-54.67	-54.27	-60.27	-55.63	-55.28	-61.3	-57.09	-56.77	-62.75
Delta	5.78	6.58	5.85	5.84	6.55	5.93	5.84	6.44	5.89
Rank	3	1	2	3	1	2	3	1	2
Σdelta	18.21			18.32			18.17		

w (%)	64.62076	65.27006	68.14355

The most suitable experimental setup for each result parameter according to the levels was obtained with NOC3HC1M3, NOC3HC1M3 and NOC3HC3M1 cases for maximum temperature, standard deviation of temperature and pressure drop under laminar flow conditions, respectively. It has been observed that the most suitable factor level sequence for pressure drop under turbulent flow conditions is NOC3HC3M1 which is the same as the laminar result. The arrangements differ for each fluid in the result parameters of the maximum temperature and the standard deviation of the temperature.

Tables 4.7 and 4.8 show the results of the ANOVA analysis for the output parameters. The effect results of all parameters were found as a result of 95% reliability test comparisons.

Table 4.7. ANOVA results for laminar flow and contribution ratios for results

Control Factors	**Water**			**EGW 25**			**EGW 50**		
	Contribution Ratios (%)								
	T_{max}	**T_{σ}**	**ΔP**	**T_{max}**	**T_{σ}**	**ΔP**	**T_{max}**	**T_{σ}**	**ΔP**
NOC	2.71	0.83	0.4	2.45	0.01	0.43	8.6	5.71	0.19
H_c	0.26	0.58	10.94	0.17	0.37	11.93	7.3	5.88	16.08
M	96.94	98.33	88.65	97.32	98.77	87.64	77.48	84.49	83.02
Error	0.1	0.25	0.01	0.02	0.85	0.01	6.62	3.91	0.7
Total	100	100	100	100	100	100	100	100	100

In the ANOVA analysis (Table 4.7), in which the effect on the result parameters was investigated under laminar flow conditions, it was found that the control factor most affecting the maximum temperature and standard deviation of temperature parameters was the flow rate and then the number of channels. The control factors affecting the pressure drop can be listed as flow rate, channel height and number of channels in order of influence.

Table 4.8. ANOVA results for turbulent flow and contribution ratios for results

Control Factors	Water			EGW 25			EGW 50		
	Contribution Ratios (%)								
	T_{max}	T_σ	ΔP	T_{max}	T_σ	ΔP	T_{max}	T_σ	ΔP
NOC	76.19	96.8	30.13	64.63	89.17	30.43	48.44	60.29	30.95
H_c	6.87	1.48	38.98	10.04	5.15	38.22	11.26	12.53	37.56
M	16.69	1.68	30.89	24.52	5.41	31.34	39.99	26.26	31.48
Error	0.26	0.04	0	0.81	0.27	0.01	0.31	0.92	0.01
Total	100	100	100	100	100	100	100	100	100

When the ANOVA results in the analyzes with turbulent flow shown in Table 4.8 are examined, it is determined that the most effective control factor for the maximum temperature and standard deviation of the temperature is the number of channels, while the effects of the control factors on the pressure drop are almost equally weighted. When laminar flow and turbulent flow are compared for the maximum temperature and standard deviation of temperature, the most effective factor in laminar flow, the flow rate has transferred the priority order to the number of channels when switching to turbulent flow.

Until this section, the result parameters were examined separately, and the best arrays were obtained according to a single parameter. However, Taguchi Based Gray Relational Analysis method was used to benefit from a single objective function to cover the effects of multiple outcome parameters.

In the first step of this method, three output parameters calculated according to the orthogonal array given in Tables 4.1 and 4.2 are normalized according to Equation (3.23) and the gray correlation coefficient (GRC) for each output parameter is calculated by applying Equations (3.23-3.26) to the normalized results (Table 4.9- 4.10). At the end of the method, the gray relational grade (GRG) was obtained by Equation (3.29). While calculating the gray relational degree, the weight coefficients (Table 4.5-4.6), which were previously found by performing the Taguchi analysis for each result parameter, were used.

Table 4.9. Normalization and Gray Relational Grade Calculation according to laminar flow results

Water								
Levels	**Normalization**			**Grey Relational Analysis**			**GRG**	**Rankings**
	T_{max}	T_{σ}	**ΔP**	T_{max}	T_{σ}	**ΔP**		
1	0.000	0.017	0.914	0.333	0.337	0.853	69.370	4
2	0.577	0.708	0.743	0.542	0.631	0.661	64.964	5
3	0.841	0.896	0.465	0.759	0.828	0.483	58.819	8
4	0.709	0.769	0.617	0.632	0.684	0.566	60.152	6
5	0.948	0.997	0.301	0.906	0.995	0.417	59.355	7
6	0.031	0.000	1.000	0.340	0.333	1.000	79.447	1
7	1.000	1.000	0.000	1.000	1.000	0.333	53.900	9
8	0.149	0.016	0.975	0.370	0.337	0.953	76.371	2
9	0.710	0.745	0.864	0.633	0.662	0.787	74.766	3
EGW 25								
Levels	**Normalization**			**Grey Relational Analysis**			**GRG**	**Rankings**
	T_{max}	T_{σ}	**ΔP**	T_{max}	T_{σ}	**ΔP**		
1	0.000	0.107	0.907	0.333	0.359	0.843	69.945	4
2	0.569	0.738	0.745	0.537	0.656	0.662	65.739	5
3	0.843	0.919	0.475	0.761	0.860	0.488	59.512	6
4	0.666	0.678	0.605	0.600	0.608	0.559	57.306	8
5	0.936	0.981	0.306	0.886	0.963	0.419	57.736	7
6	0.038	0.053	1.000	0.342	0.346	1.000	80.706	1
7	1.000	1.000	0.000	1.000	1.000	0.333	52.980	9
8	0.141	0.000	0.976	0.368	0.333	0.954	77.185	2
9	0.686	0.692	0.865	0.614	0.619	0.788	73.803	3
EGW 50								
Levels	**Normalization**			**Grey Relational Analysis**			**GRG**	**Rankings**
	T_{max}	T_{σ}	**ΔP**	T_{max}	T_{σ}	**ΔP**		
1	0.000	0.118	0.896	0.333	0.362	0.828	64.288	5
2	0.409	0.626	0.748	0.458	0.572	0.665	62.353	6
3	0.638	0.893	0.514	0.580	0.824	0.507	62.280	7
4	1.000	1.000	0.586	1.000	1.000	0.547	72.607	2
5	0.704	0.911	0.344	0.628	0.850	0.433	58.872	8
6	0.036	0.064	1.000	0.341	0.348	1.000	74.226	1
7	0.755	0.896	0.000	0.671	0.827	0.333	52.241	9
8	0.109	0.000	0.923	0.359	0.333	0.866	65.681	4
9	0.535	0.647	0.864	0.518	0.586	0.786	70.436	3

The normalization and grey relational degree calculations of the results calculated according to the laminar flow conditions are given in Table 4.9. Considering the weight factors of all the output parameters for each three fluids, the most effective cooling performance is the situation with L6 (NOC2Hc3M1) where the number of channels is 5, the channel height is 14 (mm), and the mass flow rate is 0.032 (kg/s).

Table 4.10. Normalization and Gray Relational Grade Calculation according to turbulent flow results

Water								
Levels	**Normalization**			**Grey Relational Analysis**			**GRG**	**Rankings**
	T_{max}	T_{σ}	**ΔP**	T_{max}	T_{σ}	**ΔP**		
1	0.014	0.000	0.012	0.336	0.333	0.336	33.626	9
2	0.079	0.103	0.003	0.352	0.358	0.334	34.557	8
3	0.132	0.156	0.000	0.366	0.372	0.333	35.429	7
4	0.017	0.945	0.738	0.337	0.901	0.656	45.054	6
5	0.175	0.980	0.734	0.377	0.962	0.653	47.548	5
6	1.000	0.449	0.594	1.000	0.476	0.552	84.117	3
7	0.000	1.000	1.000	0.333	1.000	1.000	56.919	4
8	0.979	0.589	0.870	0.960	0.549	0.794	90.049	1
9	0.961	0.638	0.901	0.928	0.580	0.835	89.470	2
EGW 25								
Levels	**Normalization**			**Grey Relational Analysis**			**GRG**	**Rankings**
	T_{max}	T_{σ}	**ΔP**	T_{max}	T_{σ}	**ΔP**		
1	0.017	0.000	0.001	0.337	0.333	0.334	33.597	9
2	0.070	0.122	0.000	0.350	0.363	0.333	34.412	8
3	0.123	0.179	0.000	0.363	0.378	0.333	35.300	7
4	0.020	0.850	0.736	0.338	0.770	0.655	44.818	6
5	0.165	0.908	0.740	0.375	0.844	0.658	47.361	5
6	1.000	0.247	0.517	1.000	0.399	0.508	82.891	3
7	0.000	1.000	1.000	0.333	1.000	1.000	56.487	4
8	0.984	0.566	0.749	0.969	0.536	0.666	86.305	1
9	0.962	0.622	0.763	0.930	0.570	0.679	84.220	2
EGW 50								
Levels	**Normalization**			**Grey Relational Analysis**			**GRG**	**Rankings**
	T_{max}	T_{σ}	**ΔP**	T_{max}	T_{σ}	**ΔP**		
1	0.013	0.000	0.000	0.336	0.333	0.333	33.524	9
2	0.061	0.124	0.069	0.347	0.363	0.349	34.814	8
3	0.096	0.234	0.089	0.356	0.395	0.354	35.588	7
4	0.016	0.663	0.744	0.337	0.597	0.661	43.977	6

5	0.156	0.721	0.807	0.372	0.642	0.722	48.293	5
6	1.000	0.058	0.287	1.000	0.347	0.412	81.238	2
7	0.000	1.000	1.000	0.333	1.000	1.000	54.571	4
8	0.980	0.406	0.422	0.961	0.457	0.464	80.263	3
9	0.964	0.576	0.618	0.933	0.541	0.567	81.649	1

The normalization and gray relational degree calculations of the test results with turbulent flow conditions are given in Table 4.10. Considering the weight factors of each output parameter, the most suitable cooling performance for refrigerants with 50% ethylene glycol water mixtures is L9 (NOC3Hc3M2), the channel number is 6, the channel height is 14 (mm) and the mass flow rate is 1 (kg/s). For water and EGW 25%, L8 (NOC3Hc2M1) is the case where the number of channels is 6, the channel height is 12 (mm) and the mass flow rate is 0.08 (kg/s). More mass flow rate and longer channel height are required compared to water in order to improve the cooling performance in the devices using ethylene glycol.

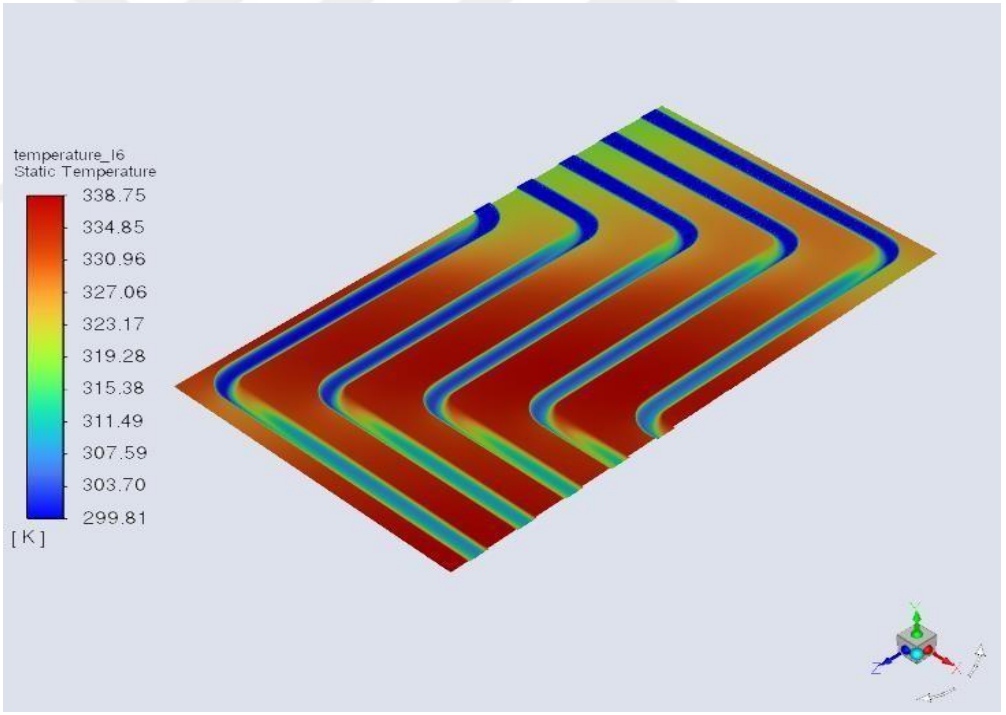
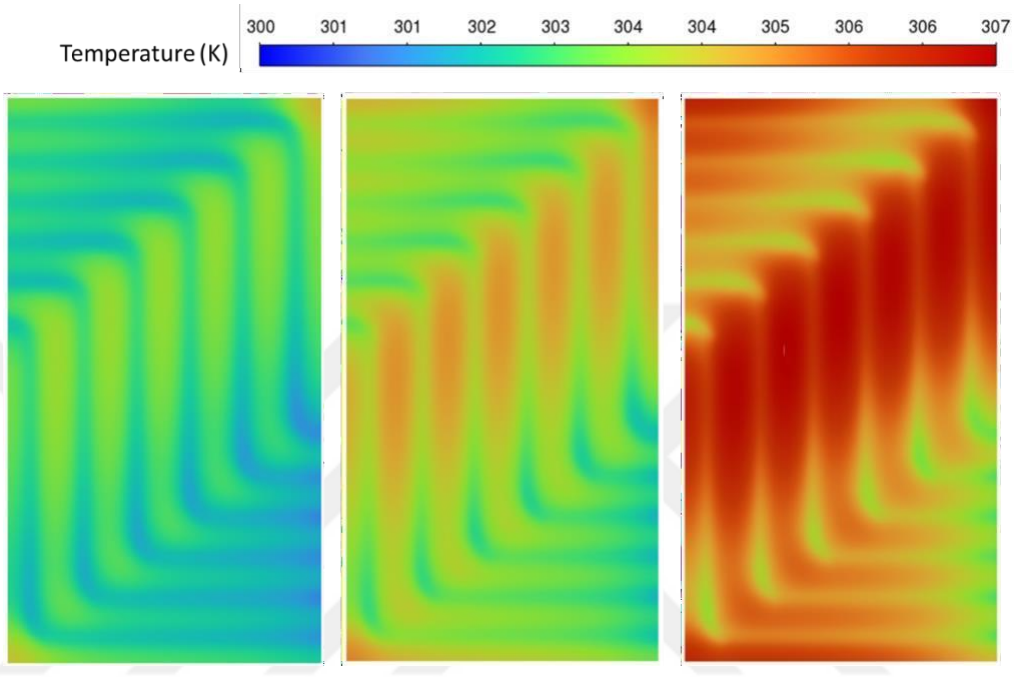


Figure 4.1. Temperature contour on water cooled heat flux surface under laminar flow condition

In Figure 4.1. the effect of the selected optimum cold plate on the heat flux surface representing the battery is shown. As expected, lower temperatures were obtained in the

region in the -x direction. which is the inlet direction of the coolant, compared to the outlet region (+x). The highest heat generation at the surface occurred in the middle regionof the battery. It has been observed that the heat transfer decreases in the middle regions due to the low pressure regions caused by the flow separations after the bends and the late reattachment of the flow with the surface.



(a) (b) (c)

Figure 4.2. Temperature distributions on the heat flux surface of the block in the arrays that give the best results **(a)** L8 for fluid water **(b)** L8 for fluid EGW 25 **(c)** L9 for fluid EGW 50

In Figure 4.2, the best results of the geometries with turbulent flow are given according to the fluid type. When the temperature distributions are compared, it is seen that the geometry cooled by water has a more uniform temperature than the others. It is seen that the uniformity deteriorates when going from fluid type water to EGW 25 and EGW 50.

5. CONCLUSION

In this study, the cooling performance of the cooling block was optimized by using different ethylene glycol ratios as the refrigerant, and the effects of channel number, channel height and total mass flow rate were investigated under laminar and turbulent flow conditions. A constant heat flux of 3020 (W/m^2) is applied to the bottom surface of the cooling block in order to model the waste heat generated by the lithium-ion battery and needs to be removed. The maximum temperature at the bottom surface, the standard deviation of the temperature on this surface, and the pressure difference arising from the fluid were selected respectively for the performance criteria of thermal resistance, temperature optimization and pump power. Each result parameter was examined separately, then a multi-response optimization study was carried out by using Taguchi-based Gray Relational Analysis Method to cover all output parameters.

In this context. the following conclusions have been made:

- While the maximum temperature and standard deviation of the temperature result parameter values obtained under turbulent flow conditions give a lower result than the values in laminar conditions due to the turbulence disrupting the thermal boundary layer due to the nature of the flow, the pressure drop also takes a higher value as expected.
- It was observed that as the ratio of ethylene glycol used in the mixture increased, the heat transfer coefficient decreased and the temperature on the bottom surface of the plate representing the surface of the battery increased in both laminar and turbulent flow characteristics.
- When the standard deviation of temperature, which is the result parameter investigated for temperature homogeneity is examined, homogeneity increases as the ethylene glycol ratio increases under laminar flow conditions, while the ratio of water and 25% ethylene glycol in turbulent conditions is close. When the 50% ratio is reached in the mixture, the standard deviation value of the temperature increases, that is, the temperature homogeneity on the surface decreases.
- It was noted that the pressure drop increased as the ethylene glycol ratio increased in both flow types.

- Weight factors showing how much each result parameter affects the cooling performance were calculated using the Minitab software with Taguchi analysis. The pressure drop with the highest variation compared to other result parameters has the highest weighting factor.
- The results obtained as a result of the Taguchi analysis performed separately for each output parameter and for both flow types differ.
- As a result of the multi-response optimization study using the Taguchi-based Gray Relational Analysis Method, which covers all output parameters and reduces them to a single response, NOC2Hc3M1 (channel number 5, channel height 14 mm and mass flow rate 0.032 kg/s), which gives the same result in every fluid for laminar flow conditions. that is, a long channel height, an average number of channels, and a low flow rate. In turbulent flow conditions, fluid percentages affect the results. It was seen that NOC3Hc2M1 gave the most suitable results for the cases where the fluid is water, and NOC3Hc3M2 for the water mixtures with ethylene glycol. While the maximum number of channels is common for both EGW values, it has been found that as the EGW ratio increases, longer channel height and more flow rate are needed to improve the cooling performance.

In this study, the effect of the cooling plate on the battery surface was investigated under laminar and turbulent flow conditions for different channel numbers, fluid types, channel dimensions and mass flow rates. Using different turbulence models and comparing the results with experimental or numerical studies and the effects of experimental studies in addition to the numerical studies may be a separate research topic in the future.

REFERENCES

Anonymous. 2019-2020. Lithium-ion Battery Market Size. Share & Trends Analysis Report By Product (LCO. LFP. NCA. LMO. LTO. NMC). By Application (Consumer Electronics. Energy Storage Systems. Industrial). By Region. And Segment Forecasts. 2022 – 2030. Address: https://www.grandviewresearch.com/industry-analysis/lithium-ion-battery-market

Anonymous. 2012. How long do greenhouse gases stay in the air? Address: https://www.theguardian.com/environment/2012/jan/16/greenhouse-gases-remain-air (Accessed on 29.01.2023).

Anonymous. 2020. Can you name the largest sources of carbon emissions in Colorado? Address: https://conservationco.org/2020/02/10/blog-colorado-largest-sources-of-carbon-emissions/ (Accessed on 29.01.2023).

Anonymous. 2021 May. Distribution of carbon dioxide emissions produced by the transportation sector worldwide in 2020. by subsector. Address: https://www.statista.com/statistics/1185535/transport-carbon-dioxide-emissions-breakdown/ (Accessed on 29.01.2023).

Anonymous. Paris Agreement. Address: https://en.wikipedia.org/wiki/Paris_Agreement (Accessed on 29.01.2023).

Anonymous 2017. Why Does CO2 get Most of the Attention When There are so Many Other Heat-Trapping Gases? Address: https://www.ucsusa.org/resources/why-does-co2-get-more-attention-other-gases#:~:text=This%20carbon%20overload%20is%20caused.accumulate%20unabated%20in%20the%20atmosphere. (Accessed on 19.02.2023).

Anonymous. Types of Lithium-ion Batteries available in the market. Address: https://inverted.in/blog/types-of-lithium-ion-batteries-available-in-the-market (Accessed on 19.02.2023).

ANSYS Meshing User's Guide. Release 2013. Page 101-117Asafa. T. B., Bryce. G., Severi. S., Said. S., A., M., Witvrouw. A., 2013. Multi-response optimization of ultrathin poly-SiGe films characteristics for Nano-Electromechanical Systems (NEMS) using the grey-Taguchi technique. *Microelectronic Engineering, Volume 111, Pages 229-233,ISSN 0167-9317, https://doi.org/10.1016/j.mee.2013.03.171.*

Bademlioglu, A., H., Canbolat, A., S., Kaynakli, O., 2020. Multi-objective optimization of parameters affecting organic Rankine cycle performance characteristics with Taguchi-Grey Relational Analysis, Renew. *Sustain. Energy Rev. 117, 109483. https://doi.org/10.1016/j.rser.2019.109483.*

Battery University. 2014. BU-205: Types of Lithium-ion. Battery University. Address : https://batteryuniversity.com/article/bu-205-types-of-lithium-ion (Accessed on 05.06.2023).

Bernardi D.. 1984 June. A General Energy Balance for Battery Systems. *J. Electrochem. Soc. 1985. Volume 132. Issue 1. Pages 5-12*

Bieker. G., Moll. C., Link. S., Plötz. P., Mock. P., 2022 March. More bang for the buck: a comparison of the life-cycle greenhouse gas emission benefits and incentives of plug-in hybrid and battery electric vehicles in Germany.

BloombergNEF, 2022. Electric vehicle outlook 2022. Address: https://bnef.turtl.co/story/evo-2022/page/1?teaser=yes (Accessed on 29.01.2023).

Chamoli. S., Yu. P., Kumar. A., 2016. Multi-response optimization of geometric and flow parameters in a heat exchanger tube with perforated disk inserts by Taguchi greyrelational analysis. *Applied Thermal Engineering, Volume 103, Pages 1339-1350, https://doi.org/10.1016/j.applthermaleng.2016.04.166.*

Chombo. P. V., Laoonual. Y., 2020. A review of safety strategies of a Li-ion battery. *Journal of Power Sources.....478. 228649. https://doi.org/10.1016/j.jpowsour.2020.228649.*

Deng. T., Zhang. G., Ran. Y., Liu. P., 2019 July. Thermal performance of lithium ion battery pack by using cold plate. *Applied Thermal Engineering. Vol. 130: 114088*

Deng. Y., Feng. C., E. J., Zhu. H., Chen. J., Wen. M., Yin. H., 2018 June. Effects of different coolants and cooling strategies on the cooling performance of the power lithium ion battery system: A review. *Applied Thermal Engineering. 142. 10–29*

E. J., Han. D., 2018. Orthogonal experimental design of liquid-cooling structure on the cooling effect of a liquid-cooled battery thermal management system. *Applied Thermal Engineering. Volume 132. Page 508-520*

Erdinc. O., Vural. B., Uzunoglu. M., 2009. A dynamic lithium-ion battery model considering the effects of temperature and capacity fading. *2009 International Conference on Clean Electrical Power. Capri. Italy. pp. 383-386. doi: 10.1109/ICCEP.2009.5212025.*

EEA. 2022 October. Address: https://www.eea.europa.eu/ims/greenhouse-gas-emission-intensity-of-1 (Accessed on 29.01.2023).

Freddi. A., Salmon. M., 2019. Introduction to the Taguchi Method. In: Design Principles and Methodologies. *Springer Tracts in Mechanical Engineering. Springer. Cham. https://doi.org/10.1007/978-3-319-95342-7_7*

Friesen. A., Horsthemke. F., Monnighoff. X., Brunklaus. G., Krafft. R., Borner. M., Risthaus. T., Winter. M., Schappacher. F., M., 2016 September. Impact of cycling at low temperatures on the safety behavior of 18650-type lithium ion cells: Combined study of mechanical and thermal abuse testing accompanied by post-mortem analysis. *Journal of Power Sources. 334. 1-11*

Gardiner. J., 2017 March. Finite Element Analysis Convergence and Mesh Independence. Address: https://www.xceed-eng.com/finite-element-analysis-convergence-and-mesh-independence/. (Accessed on 21.02.2023).

Gökçe. B.. Taǧgetiren. S.. 2009 February. Kalite ǵçin Deney Tasarımı. *Electronic Journal of machine technologies.*

Hall. N., 2021 May. Navier-Stokes Equations. NASA. Address: https://www.grc.nasa.gov/www/k-12/airplane/nseqs.html (Accessed on 21.02.2023).

Huo. Y., Rao. Z., Liu. X., Zhao. J., 2014 October. Investigation of power battery thermal management by using mini-channel cold plate. *Energy Conversion and Management 89 (2015) 387–395*

IEA. 2022. Global CO2 emissions rebounded to their highest level in history in 2021. Address: https://www.iea.org/news/global-co2-emissions-rebounded-to-their-highest-level-in-history-in-2021. (Accessed on 29.01.2023).

IEA. 2022 May. Global EV Outlook 2022 Securing supplies for an electric future.

IEA. 2022 December. Global Energy and Climate Model. IEA. Paris. Address: https://www.iea.org/reports/global-energy-and-climate-model(Accessed on 19.02.2023).

Jarret. A., Kim. I., Y., 2013 July. Influence of operating conditions on the optimum design of electric vehicle battery cooling plates. *Journal of Power Sources. 245. 644-655*

Kılıç. M.. & Yiğit. A. 2018. Isı transferi. Dora Yayın. Bursa

Kurmaev. R.. K.. Struchkov. V.. S.. & Novak. V.. V.. 2020 April. Experience in the development of an effective thermal management system for the high-voltage battery of the vehicle. *In IOP Conference Series: Materials Science and Engineering (Vol. 819. No. 1. p. 012020). IOP Publishing.*

Kweku. D. W., Bismark. O., Maxwell. A., Desmond. K. A.. Danso. K. B.. Oti-Mensah. E. A.. Quachie. A. T.. & Adormaa. B. B.. 2018. Greenhouse Effect: Greenhouse Gases and Their Impact on Global Warming. *Journal of Scientific Research and Reports. 17(6). 1–9.* https://doi.org/10.9734/JSRR/2017/39630

Jaguemont. J., Boulon. L., & Dubé. Y., 2016. A comprehensive review of lithium-ion batteries used in hybrid and electric vehicles at cold temperatures. *Applied Energy. 164. 99-114. https://doi.org/10.1016/j.apenergy.2015.11.034.*

Li. Y., & Nielsen. P. V., 2011. CFD and ventilation research. Indoor air. 21(6). 442-453.

Linderoth. J., 2021. Thermal Management of a Battery Electric Vehicle. *Chalmers University of Technology. Department of Mechanics and Maritime Sciences. Gothenburg. Sweden.*

Ma. S., Jiang. M., Tao. P., Song. C., Wu. J., Wang. J., Shang. W., 2018. Temperature effect and thermal impact in lithium-ion batteries: A review. *Progress in Natural Science: Materials International. 28(6). 653-666. https://doi.org/10.1016/j.pnsc.2018.11.002.*

Maizland. L., 2022 November. Global Climate Agreements: Successes and Failures. Address: https://www.cfr.org/backgrounder/paris-global-climate-change-agreements (Accessed on 19.02.2023).

Mann. M. E., 2022 November 15. greenhouse gas. *Encyclopedia Britannica.* https://www.britannica.com/science/greenhouse-gas (Accessed on 19.02.2023).

Moore. L., 2008 February. Greenhouse Gases: How Long Will They Last? Address: https://blogs.edf.org/climate411/2008/02/26/ghg_lifetimes/ (Accessed on 29.01.2023).

Moseman. A., Paltsev. S., 2022 October. Are electric vehicles definitely better for the climate than gas-powered cars? Address: https://climate.mit.edu/ask-mit/are-electric-vehicles-definitely-better-climate-gas-powered-cars (Accessed on 19.02.2023).

Matthe. R., Turner. L., & Mettlach. H., 2011. VOLTEC Battery System for Electric Vehicle with Extended Range. SAE International Journal of Engines. 4(1). pp. 1944-1962.

Myhre. G., Shindell. D., Bréon. F., M., Collins. W., et al., 2013. Chapter 8: Anthropogenic and Natural Radiative Forcing. Climate Change 2013: The Physical Science Basis. *Contribution of Working Group I to the Fifth Assessment Report of the Intergovernmental Panel on Climate Change. pp. 659–740.*

Ozdemir Kucuk, E., Kılıç, M., 2023. Exergoeconomic analysis and multi-objective optimization of ORC configurations via Taguchi-Grey Relational Methods. *Heliyon 2023, Vol 9, Issue 4, https://doi.org/10.1016/j.heliyon.2023.e15007.Pesaran. A., A., 2001. Battery thermal management in EV and HEVs: issues and solutions. Battery Man.43(5). 34-49.*

Panchal. S., Gudlanarva. K., Tran. M., Fraser. R., Fowler. M., 2020 April. High Reynold's number turbulent model for micro-channel cold plate using reverse engineering approach for water-cooled battery in electric vehicles. *Energies 2020. 13. 1638 ; doi:10.3390/en13071638*

Panchal. S., Khasow. R., Dincer. I., Agelin-Chaab. M., Fraser. R., Fowler. M., 2017 May. Thermal design and simulation of mini-channel cold plate for water cooled large sized prismatic lithium-ion battery. *Applied Thermal Engineering 122 (2017) 80–90.*

Park. S., & Jung. D., 2013. Battery cell arrangement and heat transfer fluid effects on the parasitic power consumption and the cell temperature distribution in a hybrid electric vehicle. *Journal of Power Sources. 227. 191-198.*

Ritchie. H., Roser. M., Rosado. P., 2020 August. CO_2 and Greenhouse Gas Emissions. Address: https://ourworldindata.org/co2-and-other-greenhouse-gas-emissions (Accessed on 29.01.2023).

Ritchie. H., 2019. Who has contributed most to global CO2 emissions? Address: https://ourworldindata.org/contributed-most-global-co2 (Accessed on 29.01.2023).

Rogelj. J., Schaeffer. M., Hare. B., 2015 Febraury. Timetables for Zero emissions and 2050 emissions reductions: State of the Science for the ADP Agreement.

Saw. L.H., Ye. Y., 2016. Computational fluid dynamic and thermal analysis of Lithium-ion battery pack with air cooling. *Applied Energy. Volume 177. 2016. Pages 783-792.*

Shang. Z., Qi. H., Liu. X., Ouyang. C., Wang. Y., 2018 October. Structural optimization of lithium-ion battery for improving thermal performance based on a liquid cooling system. *International Journal of Heat and Mass Transfer. Vol. 130. Pages 33–41. China*

Simscale., 2022 July. What is CFD | Computational Fluid Dynamics? Address: https://www.simscale.com/docs/simwiki/cfd-computational-fluid-dynamics/what-is-cfd-computational-fluid-dynamics/ (Accessed on 21.02.2023).

Slater. J., W., 2021 February. CFD Analysis Process. Address: https://www.grc.nasa.gov/www/wind/valid/tutorial/process.html#document (Accessed on 21.02.2023).

Sundén. B., 2019. Hydrogen. Batteries and Fuel Cells. *Academic Press. Chapter 6 – Thermal management of batteries. p 93-110*

Tu, J., Yeoh, G. H., Liu, C., & Tao, Y. 2023. Computational fluid dynamics: a practical approach. Elsevier.

Turaka. S., Obulu. P., Vijaya Kumar Reddy. K. 2021. Computational fluid dynamics and thermal analysis of a lithium-ion battery with different cooling system for electric vehicles. *IOP Conf. Series: Materials Science and Engineering 1136 (2021) 012033. doi:10.1088/1757-899X/1136/1/012033*

Umur. H., 2009. AkıĢkanlar Mekaniği. Dora Yayın. Bursa.

UNFCCC. What is the Paris Agreement? Address: https://unfccc.int/process-and-meetings/the-paris-agreement/the-paris-agreement (Accessed on 19.02.2023).

UNFCCC. 2015 November. Paris Agreement. *Paris Climate Change Conference.*

Ye. B., Rubel. M.R.H., Li. H., 2019. Design and Optimization of Cooling Plate for Battery Module of an Electric Vehicle. *Appl. Sci. 9. 754.*

Wakihara M., 2001. Recent developments in lithium-ion batteries. *Materials Science and Engineering. R33. Page 109-134*

Wang, X., 2019. Application of Grey Relation Analysis Theory to Choose High Reliability of the Network Node. *Journal of Physics: Conf. Series 1237. https://dx.doi.org/10.1088/1742-6596/1237/3/032056.*

Wang. J., Xu. H., 2017 July. Design and simulation of liquid cooled system for power battery of PHEV. *IOP Conf. Ser.: Mater. Sci. Eng., Volume 231. Singapore*

Wei L.C., Zhang L.Y., 2019. Experimental investigation on electro-thermal characteristics of the commercial Li-ion battery. *Earth and Environmental Science. Volume 268.*

Wei. Y., Agelin-Chaab. M.; 2019 August. Development and experimental analysis of a hybrid cooling concept for electric vehicle battery packs. *Journal of Energy Storage 25. 100906*

White. F., M., 2006. Viscous Fluid Flow. Third Edition. McGraw-Hill. New York.

Wilde. R. 2021. Population Growth and Movement in the Industrial Revolution. Address: https://www.thoughtco.com/population-growth-and-movement-industrial-revolution-1221640 (Accessed on 29.01.2023).

Woodford. C., 2022 April. Lithium-ion batteries. Address: https://www.explainthatstuff.com/how-lithium-ion-batteries-work.html. (Accessed on 19.02.2023).

Wrigley E. A 2013 March. Energy and the English Industrial Revolution. *Phil. Trans. R. Soc. A.371*. http://doi.org/10.1098/rsta.2011.0568

Wu. Z., Wang. M., Zheng. J., Sun. X., Zhao. M., Wang. X., 2018. Life cycle greenhouse gas emission reduction potential of battery electric vehicle. *Journal of Cleaner Production. Volume 190. Pages 462-470.*

Wu. W., Wang. S., Wu. W., Chen. K., Hong. S., & Lai. Y., 2019. A critical review of battery thermal performance and liquid based battery thermal management. *Energy conversion and management. 182. 262-281. https://doi.org/10.1016/j.enconman.2018.12.051.*

Xu. X., Tong. G., Li R., 2019 December. Numerical study and optimizing on cold plate splitter for lithium battery thermal management system. *Applied Thermal Engineering 167 (2020) 114787*

Ye. B., Rubel. M., R., H., Li. H., 2019 February. Design and optimization of cooling plate for battery module of an electric vehicle. *Applied Sciences. 9. 754*

Zubi. G., Dufo-López. R., Carvalho. M., Pasaoglu. G., 2018. The lithium-ion battery: State of the art and future perspectives. *Renewable and Sustainable Energy Reviews. Volume 89. Pages 292-308. ISSN 1364-0321.* https://doi.org/10.1016/j.rser.2018.03.002.